



Mechanical insight into direct singlet oxygen generation pathway: Pivotal role of FeN₄ sites and selective organic contaminants removal

Liang Zhang ^{a,b,1}, Yun Sun ^{c,1}, Rile Ge ^a, Wenhui Zhou ^a, Zhimin Ao ^{d,*}, Junhu Wang ^{a,*}

^a Center for Advanced Mössbauer Spectroscopy, Mössbauer Effect Data Center, Dalian Institute of Chemical Physics, Chinese Academy of Sciences, Dalian 116023, China

^b University of Chinese Academy of Sciences, Beijing 100049, China

^c Guangzhou Key Laboratory of Environmental Catalysis and Pollution Control, Guangdong Key Laboratory of Environmental Catalysis and Health Risk Control, Institute of Environmental Health and Pollution Control, School of Environmental Science and Engineering, Guangdong University of Technology, Guangzhou 51006, China

^d Advanced Interdisciplinary Institute of Environment and Ecology, Beijing Normal University, Zhuhai 519087, China



ARTICLE INFO

Keywords:

Fe-NC moiety
Singlet oxygen
Mössbauer spectra
High salinity condition
Density functional calculation

ABSTRACT

Herein, the systematic and novel formation pathway of singlet oxygen ($^1\text{O}_2$) on single iron atom during advanced oxidation process was investigated and revealed. Graphitic carbon matrix supported single iron atom and iron nanoclusters configurations as model catalysts were synthesized via calcinating Prussian blue, which showed admirable catalytic efficiency towards bisphenol A (BPA) oxidation even under high salinity conditions. $^1\text{O}_2$ directly generated on Fe-pyridinic N moiety bonded with terminal O of PMS (HSO_5^-) was proposed as predominant reactive species. Experimental results and theoretical analysis further detailedly demonstrated the evolutionary pathway of $^1\text{O}_2$ formation, which occurred through the interaction of two O atoms from adsorbed PMS, accompanying two HSO_4^- molecules generation with the lowest energy barrier. This study proposed novel insights into direct $^1\text{O}_2$ -modulated mechanism via Fe-N₄ configuration, providing essential atomic-scale understanding of FeNx/PMS based Fenton-like system, as well as a new strategy for the practical environmental remediation with high salinity.

1. Introduction

The increasing demand for emerging recalcitrant contaminants purification in aquatic system has drawn extensive attention owing to their high toxicity, low degradability and serious threat to ecological environment and humanity. In recent decades, by virtue of efficient refractory organic pollutants destruction, high yield of radicals and low cost of transportation and storage, persulfate-based advanced oxidation processes (AOPs) have shown enormous potential in wastewater treatment. As a typical persulfate salt with asymmetric structure, PMS can be efficiently cleaved to generate radical and nonradical species through dissociating the peroxide bond [1–3]. Nevertheless, PMS-based AOPs were identified to be susceptible to anions (Cl^- , HCO_3^- , CO_3^{2-} and natural organic matter), especially radical dominated reaction system, which objectionably quenched the active radicals to generate weaker radicals and severely inhibited the reaction activity [4,5]. Notably, by virtue of strong resistance to background substances, $^1\text{O}_2$ can overcome the disadvantages of radicals and exhibit promising application prospect for

high salinity wastewater purification. Therefore, developing nonradical (especially $^1\text{O}_2$) dominated catalytic system with excellent catalytic ability and adaptability under complex wastewater condition is still imperative.

As a selective oxidant, the long lifetime (2 μs) and moderate oxidation potential (2.2 eV) endowed $^1\text{O}_2$ with excellent reactivity towards electron-rich organic pollutant degradation such as phenol, amine and sulfide et.al [16–18]. Proverbially, several evolutionary pathways of $^1\text{O}_2$ production, including PMS self-decomposition, interaction between lattice oxygen and PMS, transformation of O_2^- and SO_5^- , and photo-excited conversion of molecular oxygen, have been intensively explored and presented in recent researches. For example, Zhang et al. pointed out that $^1\text{O}_2$ came from the direct oxidation of O_2^- via oxygen vacancy-based reaction pathway was the dominant nonradical species during PMS activation [19]. Further, Dong et al. found that sulfate radicals (SO_4^-) and peroxymonosulfate radicals (SO_5^-) were most likely to mediate the generation of $^1\text{O}_2$ [20]. However, except for the above mentioned routines, are there any novel $^1\text{O}_2$ generation

* Corresponding authors.

E-mail addresses: zhimin.ao@bnu.edu.cn (Z. Ao), wangjh@dicp.ac.cn (J. Wang).

¹ These two authors contributed equally to this paper.

mechanisms existed in PMS-AOPs system that are never reported and revealed? If there is, what is the difference between the new formation pathway and previous reported? Up to now, many researches mainly focused on the exploration of reactive metal sites in Fe-NC catalyst for the singlet oxygen generation without detailly investigating derivative pathway of $^1\text{O}_2$. For example, by comparing the PMS adsorption energy on different sites (metallic Fe, Fe-N and graphitic N), Yang et al. demonstrated that $^1\text{O}_2$ generated on single Fe-N₄ sites was crucial for the pollutant degradation and bacteria inactivation [21]. Further, Li et al. illustrated the key role of FeN₄ with low/medium spin state for the generation of $^1\text{O}_2$ through evaluating the adsorption energy of PMS on different Fe spin structures [22]. Although the significant progresses of $^1\text{O}_2$ exploration, few studies demonstrated the directly evolutionary pathway of $^1\text{O}_2$ on Fe-NC catalyst, which remains controversial and ambiguous. Meanwhile, the intermediate species was easily affected by the reaction matrix. Hence, the directly evolutionary pathway of $^1\text{O}_2$ exploration not only enrich the understanding of $^1\text{O}_2$ generation mechanism, but also overcome the deficiency of intermediate species affected by the reaction matrix and improved the utilization efficiency of PMS. It is of great significance for cost saving and improvement of complex water treatment capacity in practical application. Therefore, to tackle the current critical issue and contradiction of $^1\text{O}_2$ formation pathway, systematic clarification and verification should be further conducted in depth.

Among various transition metal-based activators [6–8], atomically dispersed metal atoms supported by nitrogen-doped carbon matrix featuring highly atomic utilization efficiency, unsaturated coordination structure and strong metal-substrate interaction can overcome the disadvantage of inhomogeneity of metal sites and exhibit robust catalytic performance in various catalysis fields, such as electrocatalytic oxygen reduction [9–11], photocatalysis [12] and NO selective reduction [13] et.al. Likewise, benefiting from the merits of homogeneous and heterogeneous catalysts, the iron-based Fe-NC configuration have shown tremendous potential in environment remediation. For instance, Gao et al. reported the utilization of Fe-NC catalyst with Fe-pyridinic moiety achieved excellent organic pollutants oxidation during PMS activation process [14]. Further, He et.al developed a novel carbon nanocubes with abundant well-dispersed FeN_x sites to achieve superb activity for phenol degradation via activating PMS [15]. Despite the excellent reaction efficiency of Fe-NC based catalyst in PMS-based AOPs application, the valid evidence and underlying detailed formation route of reactive species via Fe-N moieties are still under debate.

Inspired by the above recapitulative analysis, in this work, Fe-based catalyst with Fe-NC and other Fe configurations (iron oxides and metallic iron) was fabricated via facile calcination strategy. The synthetic catalysts delivered admirable catalytic activity in PMS activation for refractory pollutant degradation even under high salinity, high concentration of humic acid and wide pH range. Especially, the concentration of high salt wastewater in this work has refreshed the limit of current researches, which showed excellent environmental resistance. Based on the quenching experiments EPR analysis, $^1\text{O}_2$ was confirmed as the predominant reactive specie, which was directly generated on reactive Fe-pyridinic N moieties boned with terminal O atom of PMS. In addition, experimental results and density functional theory (DFT) calculation detailly revealed the validity and rationality of direct generation routine of $^1\text{O}_2$, which was derived from the two O atoms on adsorbed HSO₅⁻ accompanying two HSO₄⁻ molecules formation. This work would give essential insights and guidance for the understating of direct $^1\text{O}_2$ formation mechanism in Fe-NC/PMS system.

2. Experimental section

2.1. Chemicals

The chemicals used in this study were presented in [Supporting Information](#) (Text S1).

2.2. Synthesis of PB and Fe-NC catalysts

Firstly, 40 mL, 5 mM K₃[Fe(CN)₆] was dropped into a solution of 5 mM FeCl₃ (40 mL) and then reacted for 30 min under vigorous stirring condition. Subsequently, the mixture was aged under dark condition for 72 h. After that, the supernatant was removed and the precipitate was washed three times using deionized (DI) water and ethanol, and dried in oven at 60 °C for 12 h.

As for the preparation of Fe-NC catalysts, in brief, a certain amount of PB was fully mixed and grinded with melamine in agate mortar. Then, the as-prepared powder was transformed into porcelain boat and heated to 600 °C at 2 °C min⁻¹ under N₂ atmosphere for 3 h. After cooling to room temperature, the mixture was sunk into H₂SO₄ solution (1 M) and kept in a water bath at 80 °C for 24 h. Finally, the obtained mixture was washed with DI water until neutral and then dried at 60 °C for 12 h. A series of Fe-NC catalysts with different mixing ratio (Melamine/ PB = 1, 3, 5, 7, 10) were named as MP-1, MP-3, MP-5, MP-7, MP-10, respectively. For comparison, the pure melamine without addition of irons source and PB without addition of melamine were pyrolyzed using the same method as denoted as CN and MP-0 [Scheme 1](#).

2.3. Characterization

Detailed characterization information was shown in [Supporting information](#) (Text S2).

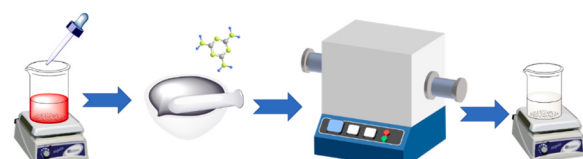
2.4. Evaluation of Fenton-like performance

The organic pollutant and PMS solution were prepared and stored in dark condition. All reactions were exposed in air condition and conducted in room temperature. Firstly, a certain amount of catalyst (30 mg) was added into 100 mL pollutant solution (100 μM) and stirred in dark condition for 30 min to achieve equilibrium of adsorption-desorption. Then, the experiment was initiated by adding 0.5 mL 61.4 g L⁻¹ PMS oxidant solution. During the reaction, an appropriate amount of suspension was withdrawn, filtered with 0.22 μm filter membranes and immediately quenched with 0.2 M sodium sulfite solution. The concentration of pollutant was analyzed using high-performance liquid chromatography (LC-2030 SHIMADZU, Japan). Detailed analysis parameters were listed in [Table S1](#). For the stability and reusability test, the used catalyst was washed thoroughly with methanol and DI water after each cycle and then dried at 60 °C for next consecutive usage.

3. Results and discussion

3.1. Characterization of catalyst

The thermal behavior of precursor (PB/melamine = 1:3) was firstly investigated using thermogravimetric measurement ([Fig. S1](#)). The weight loss occurred at first stage (below 200 °C) and second stage (200–300 °C) was mainly due to the removal of crystalline water and coordinated water, while a continued decrease at the third stage (over 300 °C) was attributed to the decomposition of organic ligands (C≡N) in PB and melamine [23]. When the temperature was elevated to 600 °C, the thermal decomposition was almost complete and further improve pyrolysis temperature would result in aggregation and iron carbide



Scheme 1. Schematic synthesis route of Fe-NC catalysts.

formation. Herein, to achieve an optimal thermal behavior, the calcination temperature was fixed at 600 °C and a series of Fe-NC catalysts were obtained. Afterwards, X-ray diffraction (XRD) patterns of synthetic catalysts were investigated and shown in Fig. 1a. All Fe-NC catalysts exhibited the similar structural information with pure CN sample obtained by calcining pure melamine (Fig. S2) and no characteristic peak assigned to iron carbide and oxide can be observed. Meanwhile, the intensity of (002) peak ascribed to graphene (JCPDS No. 01-1578) gradually enhanced with increase of mass ratio between melamine and PB, which was attributed to the promoted crystallinity of graphitic carbon. The type IV N_2 adsorption-desorption isotherms with H3 hysteresis loop indicated the mesoporous architecture of Fe-NC catalysts, which was conducive to the rapid diffusion between pollutant and full exposure of active sites during catalytic process (Fig. 1b). The corresponding BET specific surface area of MP-1,3,5 samples were calculated to be 46.91, 52.72 and 48.81 $m^2 g^{-1}$, respectively. The pore size distribution curves further illustrated the meso-porosity of MP catalyst with the average pore diameters of 2.25, 2.97 and 3.14 nm (Table S2). Besides, the morphology of Fe-NC catalyst was investigated using TEM measurement, as shown in Fig. 1c-d. The existence of a large number of hollow vesicle structure implied the defective and porous carbon substrate in Fe-NC catalyst. More importantly, no clearly visible particles and lattice fringes can be detected in HR-TEM images, suggesting that iron species mainly existed in nanoclusters or atomically distributed on the N-doped carbon layer. In order to confirm the present form of Fe, the HAADF-STEM of MP-3 was employed and shown the bright spots corresponding to iron atoms were distributed in N-doped carbon matrix

with some clusters (Fig. 1e-f). Notably, the iron particles were not observed on the MP-3. HAADF-STEM mapping images suggested the Fe, N, C were uniformly scattered on the carbon layers (Fig. 1g-j). This was consistent with the above characterization results, suggesting iron clusters and iron single atom coexisted in MP-3. Moreover, Raman spectroscopy was conducted to explore the structural defects in carbon-based materials with observation of graphitic structure (D band, 1342 cm^{-1}) and in-plane vibration mode of sp^2 graphitic carbon (G band, 1578 cm^{-1}) [20,24]. As depicted in Fig. S4, the calculated defective degree (I_D/I_G) of MP-1, MP-3 and MP-5 were determined to 1.03, 0.90 and 0.84, respectively. Apparently, with decreasing the mixing amount of melamine, the gradually increased I_D/I_G value revealed the more generated defects derived from insufficient N and C source in melamine. The defect-rich structure could accelerate electron transfer from electron-rich pollutant to PMS oxidant and thus promote the organic catalytic process [24]. Therefore, I_D/I_G value may be relaxed with catalytic performance in MP-3/PMS system and the possible electron transfer mechanism should be considered in subsequent studies.

In order to verify the valence state and coordination environment of Fe species in MP-1, MP-3 and MP-5, X-ray absorption spectroscopy at Fe K-edge was measured with the FePc and Fe foil reference. As shown in Fig. 2a, the Fe K-edge XANES spectra of MP-1, MP-3 and MP-5 were located between Fe foil and FePc, indicating the valence states were higher than Fe^0 and close to Fe^{2+} . This result demonstrated the metallic Fe specie was existed in MP-1, MP-3 and MP-5. The k^3 -weighted Fourier transformation of Fe K-edge from extended X-ray absorption fine structure (EXAFS) spectra for these catalysts were further analyzed, and

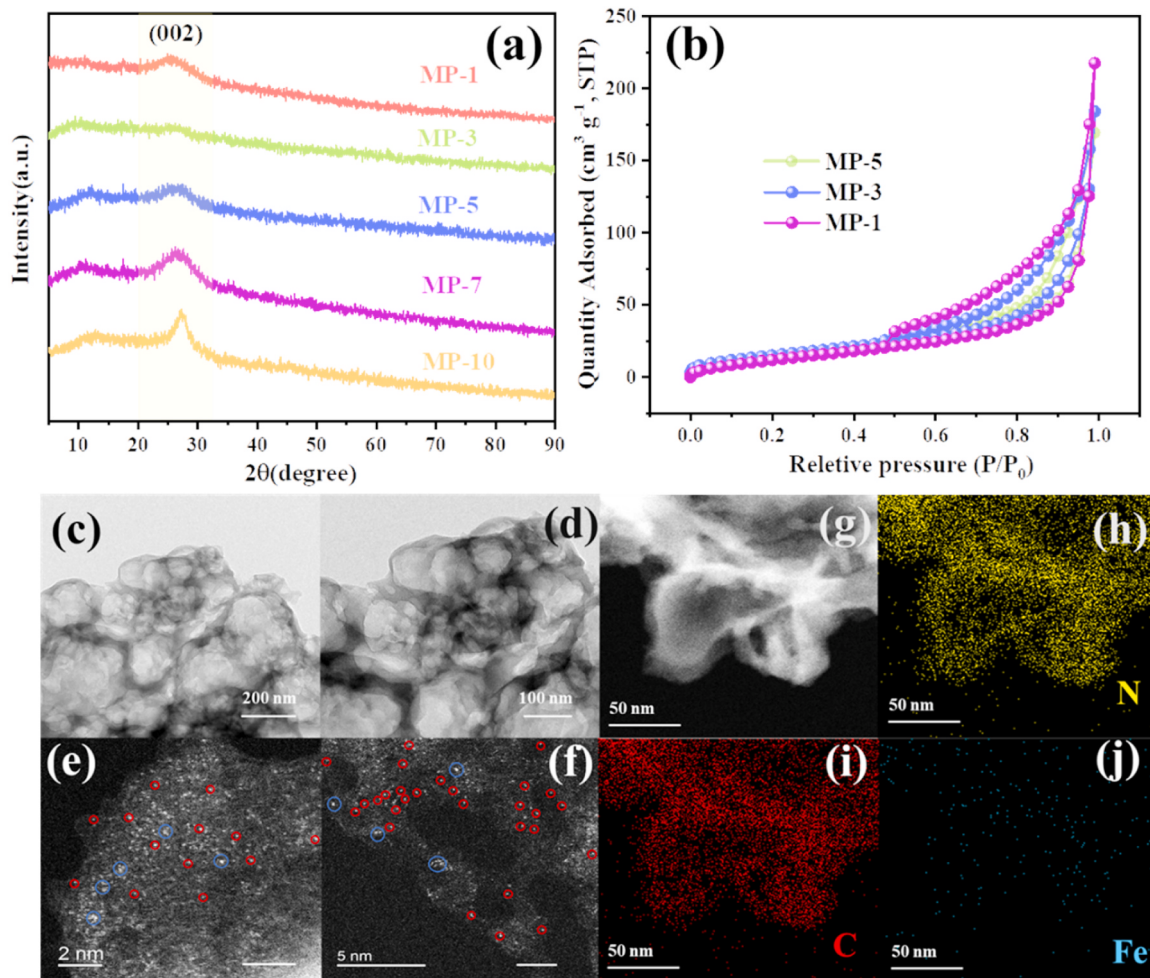


Fig. 1. XRD patterns (a) and N_2 adsorption-desorption isotherm (b) of Fe-NC catalysts; TEM images (c-d) and HAADF-STEM images (e-f) of MP-3; HAADF image (g) and corresponding EDS images (h-j) of MP-3.

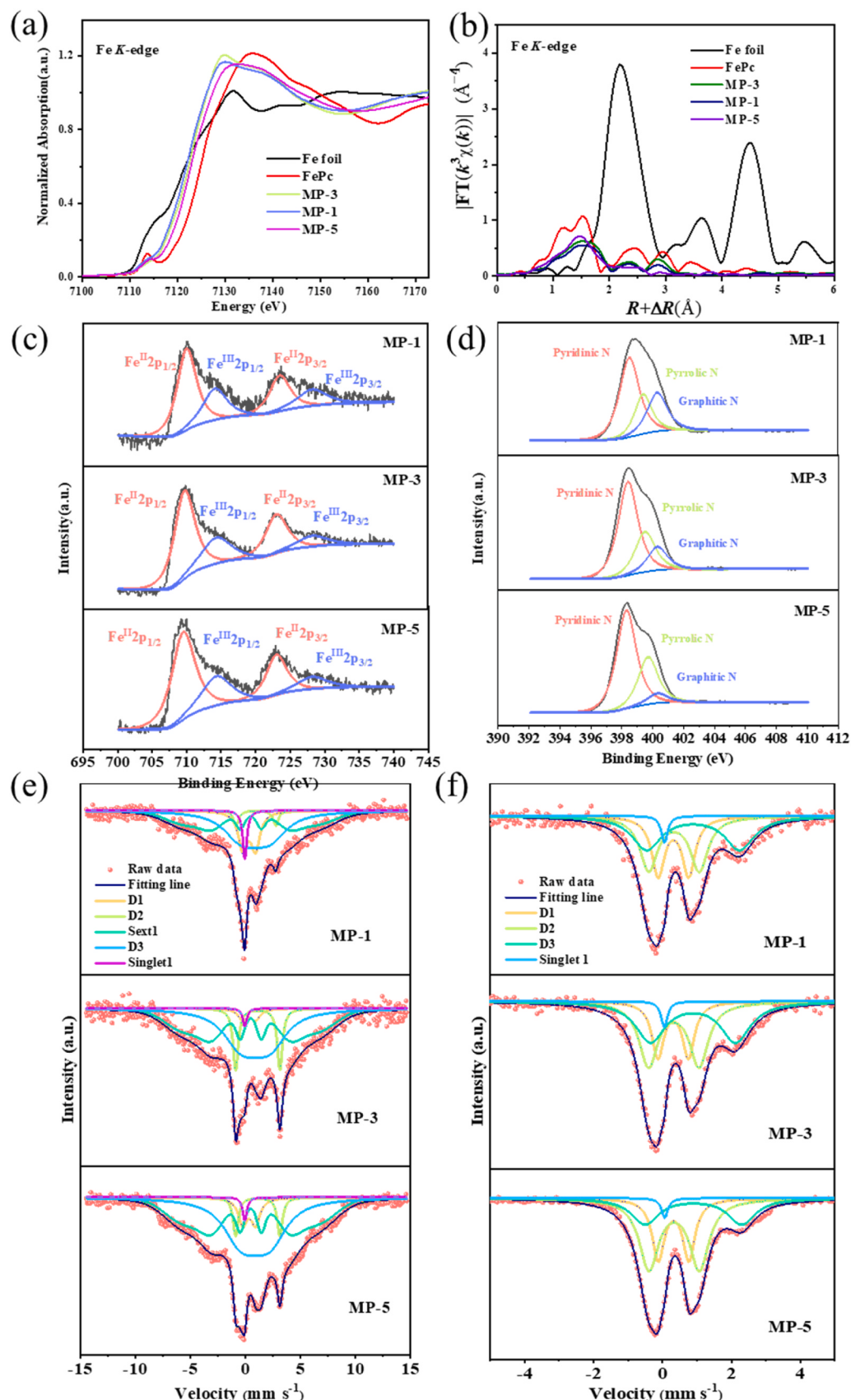


Fig. 2. K-edge XANES spectra of MP-1, MP-3, MP-5, Fe foil, FePc (a); Fourier transforms of the k^3 -weighted K -edge EXAFS spectra of MP-1, MP-3, MP-5, Fe foil, FePc (b); High resolution XPS (a) Fe 2p spectra (b) N 1s spectra of MP-1, MP-3 and MP-5 catalysts; (c) Low - temperature and (d) Room - temperature ^{57}Fe Mössbauer spectra of MP-1, MP-3 and MP-5 catalysts.

the corresponding fitting results were summarized in Table S3. As shown in Figs. 2b and S5, the EXAFS results indicated the first shell peaks located at ~ 2 Å can be assigned to Fe-N moiety. The average coordination number of MP-3 were ~ 4 , confirming the existence of FeN_4 configuration. Furthermore, the peak at 2.59 Å was attributed to Fe-Fe bond and similar structure was also found in MP-1 and MP-5 catalysts, suggesting the presence of metallic Fe species, which was well consistent with the results of HAADF-STEM in Fig. 1e-f. Overall, the metallic Fe species and single atom Fe species both coexisted in the MP-1, MP-3 and MP-5 catalysts.

XPS survey spectra was performed to investigate the bonding character and element composition of MP-1, MP-3 and MP-5 catalysts (Fig. 2c-d). Expectedly, the signal of metallic iron was not detected in all Fe-NC catalysts, which can hypothesize that metal iron on the catalyst surface was totally dissolved and removed during acid treatment and atomically distributed Fe-NC was dominant configuration (Fig. 2c). The diffraction peaks located at around 709.7 eV and 714.3 eV can be assigned to $\text{Fe}^{II} 2p_{1/2}$ and $\text{Fe}^{III} 2p_{1/2}$ of Fe-NC configuration. As shown in Table S4, the highest Fe content was obtained by MP-3 catalyst, which indicated that appropriate amount of melamine can provide adequate nitrogen and carbon sites to bond with iron sites and achieve stable and atomic distribution of iron atoms on N-C matrix. As for the N 1 s XPS spectra (Fig. 2b and Table S5), the characteristic peaks centered at 398.4, 399.6 and 400.1 eV were assigned to pyridinic N, pyrrolic N and graphitic N, respectively. It was demonstrated that the distortion of carbon network can form graphitic N and generate defective site for the cleavage of O-O bond during PMS activation [19]. However, by introducing higher amount of melamine into precursor, the relative proportion of graphite nitrogen species decreased from 25% to 6%, illustrating that excessive melamine was not conducive to graphitization process of carbon-based materials and thereby suppressing the reactive sites formation.

To further identify the Fe-NC configuration and unveil sophisticated metal coordination environment in MP catalysts, ^{57}Fe Mössbauer spectroscopy was recorded under room temperature (297 K) and low temperature (6.5 K). As a sensitive characterization of microstructure and magnetic ordering analysis in iron-based catalyst, Mössbauer spectrum can provide hyperfine information around metal center microstructure, including oxidation state, spin state and hyperfine magnetic fields, through detecting the resonant γ -rays absorption of nuclear transition from ground state to excited state [25]. On the basis of ^{57}Fe Mössbauer spectra (Fig. 2e-f) and hyperfine fitting parameters (Table S6), three doublets (D1-D3) assigned to different iron components and one singlet assigned to superparamagnetic iron nanocluster [26] can be observed in Fe-NC catalysts under room temperature, ruling out the existence of large-size iron particles and iron carbide species. The iron components corresponding to D1, D2 and D3 were assigned to Fe_2O_3 or LS (low spin) $\text{Fe}^{II}\text{N}_4/\text{C}$ or HS (high spin) $\text{Fe}^{III}\text{N}_4/\text{C}$ [27–30] and FeN_4 center similar to $[\text{FePc}]^{2-}$ moieties [26,28] and ferrous high-spin FeN_4 site [27,31], respectively. However, with the appearance of magnetic hyperfine splitting parameter similar with iron oxides/carbide, an emerging sextet curve was detected with isomer shift value of 0.49 mm s^{-1} , which was not observed under room temperature [32]. The nanocluster of iron oxide/carbide that is magnetic at LT Mössbauer spectra will have a doublet spectrum at RT Mössbauer spectra that is likely to overlap with the D1 doublet. Previously, Herrera et al. pointed out that magnetic hyperfine splitting of nanoscale iron cluster cannot be easily found at ambient condition due to the faster fluctuation of cluster moments than nuclear Larmor precession above spin class freezing temperature [33, 34]. Likewise, Suzdalev reported that even under 78 K, the magnetic hyperfine splitting property of iron oxide nanocluster still cannot be detected using highly sensitive Mössbauer spectroscopy [35]. In this work, similarly, owing to the acid etching process, the large particles on Fe-NC catalyst surface were totally removed, while the extremely negligible iron species warped by carbon matrix may be preserved, resulting in the appearance of magnetic hyperfine splitting parameters

under extremely low temperature. In order to identify the existence of these iron species, the Fe-NC was obtained through direct calcination of PB and was characterized by ^{57}Fe Mössbauer spectroscopy. As shown in Fig. S6, Fe_3C , α -Fe and Fe_5C_2 were still observed after acid-washing, indicating the magnetic hyperfine splitting of MP-3 catalyst was derived from metallic iron and iron oxide/carbide species and abundant carbon and nitrogen source generated from melamine facilitate the formation of Fe-N sites. Meanwhile, the relatively low iron concentration around 0.99, 1.47 and 1.16 wt% in MP-1, MP-3 and MP-5 catalysts obtained by ICP-OES measurement (Table S8) further authenticated the hypothesis of tiny nanocluster existence.

3.2. Persulfate activation performance

The catalytic performance of Fe-NC catalysts was evaluated using bisphenol A (BPA) as target pollutant. As shown in Fig. 3a, in the presence of PMS, BPA degradation over CN sample can be negligible. As for the MP catalysts, 95% BPA can be removed within 10 min, signifying the admirable catalytic capacity and crucial role of Fe-NC configuration in PMS conversion. The corresponding pseudo-first-order apparent reaction rate constants (k) of MP-1, MP-3, MP-5, MP-7 and CN catalysts were calculated to be 0.26, 0.29, 0.20, 0.17 and 0.007 min^{-1} , respectively (Fig. 3b). Among them, MP-3 catalyst exhibited the optimal catalytic performance, which exceeded CN by 2 orders of magnitude at identical reaction condition. For comparison, the removal behavior of BPA by the adsorption ability under dark condition and individual PMS appeared to be rather limited (Fig. S7a-b). The total leached iron concentration was monitored during catalysis process and the corresponding control homogenous experiment using the equal leached Fe^{2+} ions concentration was also explored (0.14 mg L^{-1}). Expectedly, the inappreciable BPA removal efficiency in homogeneous $\text{Fe}^{2+}/\text{PMS}$ system excluded the contribution of leached iron species and further validated the crucial effect of heterogenous iron sites towards PMS activation and organic decontamination (Fig. S7c). To better describe catalyst reactivity, the specific catalytic activity (pseudo-first-order apparent reaction rate constant normalized to the dosage and BET surface area) of catalyst was calculated. As depicted in Fig. S8a and Table S8, the intrinsic activity of MP-3 was significantly superior than other catalysts reported to date, manifesting the excellent potential as an PMS activator for recalcitrant contaminant purification, which was adopted as the representative catalyst in subsequent experiments.

The pH value is regarded as the most sensitive parameter during Fenton-like reaction. Generally, the addition of PMS can give rise to an obvious decline of solution pH and hinder the precise evaluation of acid-based environment [36]. To avoid this phenomenon, three buffer solutions with different pH values were adopted. As shown in Fig. S8b, MP-3/PMS system can achieve efficient oxidation ability under a wide pH range. Compared with acidic and neutral conditions, the alkaline microenvironment with pH = 9.18 exhibited the optimal catalytic performance. This was because, on the one hand, excessive H^+ would bond with PMS and ROS and thereby suppressed the catalytic kinetics. On the other hand, alkaline condition could initiate nucleophilic attack of PMS (SO_5^{2-}) to generate peroxide oxygen of PMS (HSO_5^-), which was conducive to associated $^1\text{O}_2$ and high valent metal complexes production [4]. Further, additional operating parameters including catalyst dosage, BPA and pollutant concentration were also evaluated and shown in Fig. S8c-h. In summary, the optimal reaction performance can be achieved with the addition of 1 mM PMS, 300 mg L^{-1} catalyst and $100 \mu\text{M}$ BPA.

3.3. Reactive species involved in BPA degradation

3.3.1. Excluding free radical pathway

Hydroxyl and sulfate radicals ($\cdot\text{OH}$ and $\text{SO}_4^{\cdot-}$) are generally reported as the dominant reactive oxygen species in persulfate-based AOPs. Herein, the free radicals involved in Fe-NC/PMS system were

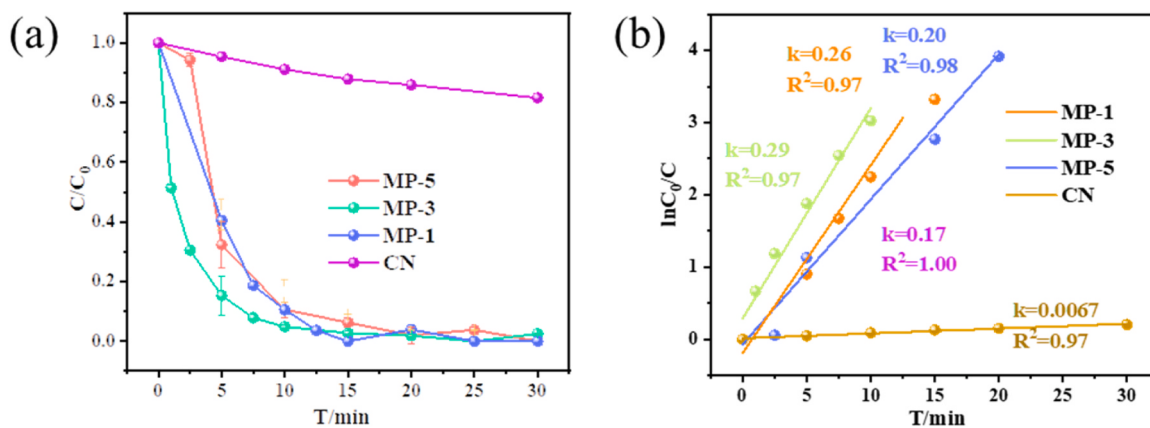


Fig. 3. Degradation of BPA in different systems (a); the corresponding pseudo-first order kinetics curves (b); (Conditions: [BPA] = 100 μM , [PMS] = 1 mM; [Catalyst] = 300 mg L^{-1}).

investigated by quenching experiments and EPR measurement. Firstly, TBA ($k_{\text{OH}} = 3.8\text{--}7.6 \times 10^8 \text{ M}^{-1} \text{s}^{-1}$) and MeOH ($k_{\text{OH}} = 9.7 \times 10^8 \text{ M}^{-1} \text{s}^{-1}$; $k_{\text{SO}_4^-} = 1.6 \times 10^7 \text{ M}^{-1} \text{s}^{-1}$) were employed as typical quenching agents to distinguish the existence of $\cdot\text{OH}$ and SO_4^\cdot radicals [37]. As shown in

Figs. 4a and S9a, the addition of TBA and MeOH did not give rise to obvious influence on pollutant degradation efficiency in MP-3/PMS system. Meanwhile, the similar phenomenon in solvent change experiment (substitution H_2O by MeOH solvent) ruled out the contribution

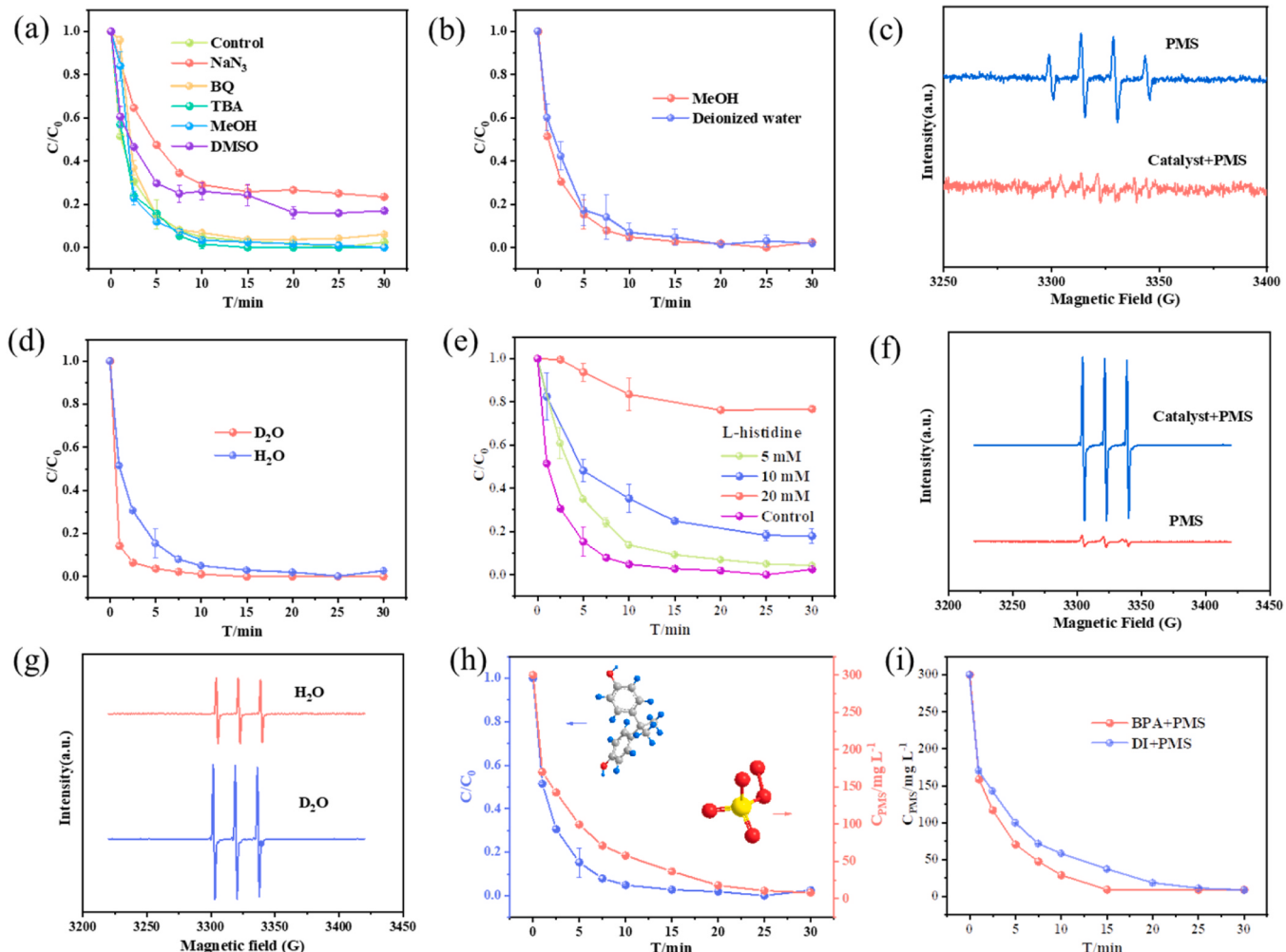


Fig. 4. Fenton-like activity towards BPA degradation by MP-3 catalyst with different quenching agents (a); BPA degradation of MP-3/PMS/BPA with methanol as solvent (b); EPR spectra for DMPO-OH/DMPO- SO_4 of different system (c); BPA degradation of MP-3/PMS/BPA with D_2O as solvent (d); Quenching effect of different concentration of L-histidine (e); EPR spectra of $\text{TEMP}^{-1}\text{O}_2$ in MP-3/PMS and PMS alone systems (f); EPR spectra of $\text{TEMP}^{-1}\text{O}_2$ in the different systems with D_2O and H_2O as solvent (g); Decomposition rates of PMS and BPA in MP-3/PMS/BPA system (h); Decomposition rates of PMS in MP-3/PMS/BPA system and MP-3/PMS system (i). (Conditions: [BPA] = 100 μM , [PMS] = 1 mM; [Catalyst] = 300 mg L^{-1}).

of-OH and $\text{SO}_4^{\cdot-}$ radicals (Fig. 4b). Likewise, the DMPO-trapped EPR spectra displayed much weaker characteristic quartet line with an intensity ratio of 1:2:2:1 (symmetry center : $g = 2.0055$, $a_{\text{N}} = 14.9 \text{ G}$, $a_{\text{H}} = 14.9 \text{ G}$) in MP-3/PMS system than that of PMS alone system, further excluding the reactive impact of-OH and $\text{SO}_4^{\cdot-}$ radicals (Fig. 4c).

3.3.2. Non-radical mediated mechanism

NaN_3 was chosen as a quencher by virtue of high second-order rate constant ($k_{1\text{O}_2} = 1 \times 10^9 \text{ M}^{-1} \text{ s}^{-1}$) to identify the formation of ${}^1\text{O}_2$ non-radical species. As shown in Fig. S9a, the reaction rate constant was apparently inhibited from 0.29 to 0.091 min^{-1} after adding 10 mM NaN_3 . However, it was reported that PMS oxidant can be rapidly depleted by NaN_3 and the consequence of declined reaction efficiency may confuse the contribution of ${}^1\text{O}_2$ species. Therefore, L-histidine ($k_{1\text{O}_2} = 3.2 \times 10^7 \text{ M}^{-1} \text{ s}^{-1}$) and D_2O ($k_{\text{D}2\text{O}} = 1.5 \times 10^4 \text{ s}^{-1}$) with distinct quenching capacity and prolonged lifetime of ${}^1\text{O}_2$ were applied. As shown in Fig. 4d-e, the dramatically suppressed reactive rate constant ($0.29\text{--}0.015 \text{ min}^{-1}$) in the presence of 20 mM L-histidine and obviously enhanced catalytic activity and signal intensity of TEMP- ${}^1\text{O}_2$ adducts under D_2O system compared with H_2O validated the crucial role of ${}^1\text{O}_2$ in MP-3/PMS system (Figs. S9b and 4g). Moreover, as the reaction proceeded, the gradual decreased ${}^1\text{O}_2$ intensity implied the steady participation and consumption in BPA oxidation process. (Fig. S9c).

Besides, nonradical oxidation process with high-valent metal complex and electron-shuttling mechanism as mainly catalytic pathways were reported during PMS/PDS activation [38,39]. Herein, DMSO, PMSO probes and electrochemical measurements were carried out to unveil the possible existence of these nonradical pathways in MP-3/PMS system. As depicted in Fig. 4a, the introduction of DMSO subsequently suppressed the catalytic kinetic from 0.29 to 0.22 min^{-1} , implying the possible generation and involvement of high-valent iron species. Benefiting from the oxygen atom transfer reaction, PMSO consumption and PMSO_2 generation were monitored using ACQUITY ultra high liquid chromatography-mass spectrometry (LC-MS) to identify this hypothesis. As shown in Fig. S10a-b, the molecules with $m/z = 140.9$ and $m/z = 157.1$ were clearly observed under positive detection mode, which correspond well to the standard PMSO and PMSO_2 references. Moreover, two mass units with $m/z = 174.2$ and 329.9 assigned to $[\text{M}+\text{NH}_4]^+$ and $[\text{2 M}+\text{NH}_4]^+$ ($\text{M} = \text{PMSO}_2$) and an additional $m/z = 79.0$ ascribed to the cleavage of a benzene ring from PMSO_2 were also detected in MS spectrum, indicating the transformation of PMSO to PMSO_2 by the generated high-valent iron species (Fig. S10c-d). Additionally, with extension of reaction time, the gradually improved characteristic peak intensity of PMSO_2 accompanied by the decreased PMSO concentration in MP-3/PMS system (Fig. S11a-b) was distinctly different from PMS alone system with less PMSO_2 production (Fig. S11c-d). These results collectively authenticated the high valent iron species (Fe (VI/V = O) formation using MP-3 catalyst as an efficient PMS activator.

Further, the electron-shuttling mechanism was investigated using electrochemical measurements and oxidant consumption experiment. Compared with sole MP-3 system in the absence of PMS, the increased current intensity of linear sweep voltammetry (LSV) in MP-3/PMS system demonstrated the formation of metastable PMS complexes via the direct interaction between oxidant and catalyst. Besides, the addition of BPA could promote the electron transfer and intrigue an increase of current density (Fig. S12a). It can be speculated that BPA as the electron donor can react with the surface-confined nonradical species and achieve efficient decomposition. Afterwards, the potential of MP-3 and CN catalyst surface was measured by in-situ open-circuit voltage with addition of PMS followed by BPA. As shown in Fig. S12b, the introduction of BPA had a negligible impact on the open-circuit potential, while the subsequent introduction of PMS provoked a dramatical potential increase, implying the strong electron transfer occurred between catalyst surface, PMS and BPA. Notably, compared with CN material, the pronounced improvement of potential in MP-3 catalyst system evidenced the accelerated electron-shuttling by essential metal sites.

Electrochemical impedance spectroscopy (EIS) revealed that MP-3 catalyst possessed the smallest arc radius and minimal resistance to carrier transfer (Fig. S12c), which was conducive to decreasing the electrochemical impedance of electron and accelerating charge transfer from catalyst to solid/liquid interface to participate into the oxidation reaction. Subsequently, the consumption of PMS concentration was measured with or without BPA during the reaction process. As shown in Fig. 4h-i, the synchronous tendency between BPA degradation and PMS consumption indicated that PMS was an indispensable driving force for pollutant oxidation. Compared with MP-3/PMS system without BPA, the addition of BPA effectively accelerated the consumption rate of PMS, which was consistent with previous reported catalytic electron-shuttling processes [40–43]. Collectively, it can be concluded that ${}^1\text{O}_2$ was the primary active specie in the MP-3/PMS/BPA system, while high-valent iron complex and electron-shuttling pathway played indispensable effect in catalysis reaction.

3.4. Mechanistic insights into PMS activation over MP catalyst

3.4.1. Potential active sites

Different configurations including Fe-N-C, metallic iron, pyridinic N, pyrrolic N, graphitic N and graphitic carbon were coexisted in MP-3 catalyst. In comparison with pristine CN, the integration of iron sites effectively boosted the catalytic efficiency from 0.007 min^{-1} to 0.29 min^{-1} . Meanwhile, the presence of sodium oxalate ($\text{Na}_2\text{C}_2\text{O}_4$), a chelator of Fe ion, significantly depressed the BPA removal efficiency, further confirming the essential role of iron species for organic compounds oxidation (Fig. S13a) [44]. To further reveal the role of different iron coordination structures, correlation analysis between catalytic efficiency and different iron species content was carried out. As depicted in Fig. S14a-d, according to results of room-temperature/low temperature ${}^{57}\text{Fe}$ Mössbauer spectra and ICP-OES, the best positive correlation ship between Fe-NC configuration and reaction efficiency was obtained, revealing the vital role of Fe-NC moieties as promising catalytic descriptors for PMS activation. In addition, phenanthroline (Phen), a trapping agent for Fe-NC moieties, was selected to evaluate the role of Fe-NC in reaction process. As shown in Fig. S13b, the addition of Phen severely inhibited the reaction efficiency, which was consistent with the result of correlation ship.

Recently, pyridinic N, pyrrolic N and graphitic N were also reported to be the potential active sites during PMS activation process. Herein, the nitrogen species and the variation of N component before and after reaction were evaluated. Fig. S15 indicated that only the proportion of graphitic N slightly declined after the reaction (17–8%), while pyrrolic N content increased and pyridinic N ratio remained relatively constant. This phenomenon may be attributed to the modulation of electron distribution near graphitic N and thus improved the adsorption capacity of negatively charged PMS molecule on the positively charged carbon matrix [45]. To identify this, DFT calculation was conducted and the corresponding electrostatic potential map of N-doped graphene (Fig. 5a) indicated that graphitic N was more likely to attract the electron from neighboring C atoms and exhibited higher electron density, which possess strong affinity and activation capacity towards PMS molecule. Nevertheless, no strong positive correlation between N species and kinetic constant (Fig. 5b) can be observed, excluding the responsibility of N species for efficient catalysis process.

To further analyze the surface chemical evolution process, low-temperature EPR measurement was carried out, which can provide detailed information of iron species with half-integer spin and potential presence of high valent iron components during redox reaction [46,47]. As shown in Fig. 5c, an isotropic signal at $g = 4.2686$ indicated the existence of high-spin Fe^{III} species in Fe-NC/ H_2O system. Evidently, the improved intensity of ferric (Fe^{III}) ions signal in the presence of PMS illustrated the accelerated redox $\text{Fe}^{\text{II}}/\text{Fe}^{\text{III}}$ conversion, which provided solid evidence of dominant Fe-NC configuration towards Fenton-like catalytic reaction. Additionally, an isotropic signal at $g = 2.0028$ can

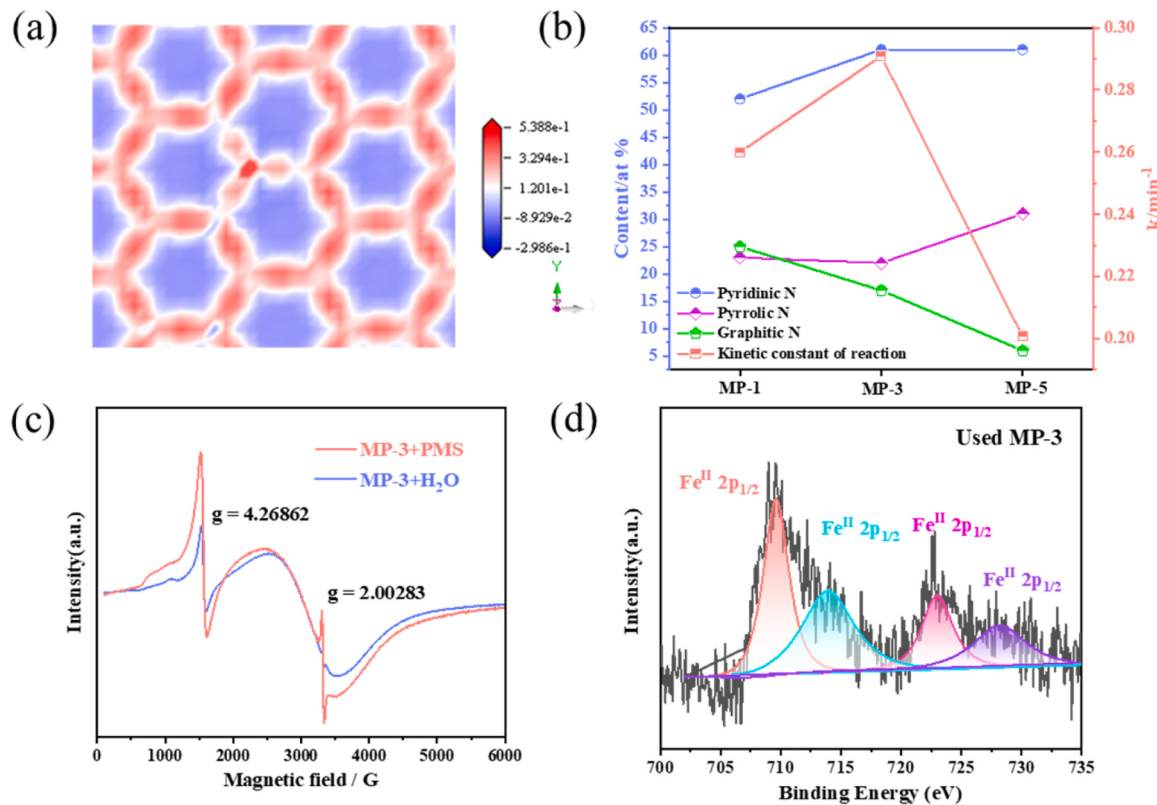


Fig. 5. Electrostatic potential map of N-doped graphene (a); Relationship between different N species content and kinetic constant of reaction of as-synthesized catalysts (b); Low temperature EPR of MP-3/PMS and MP-3/H₂O (c); XPS analysis of used MP-3 (d). (Conditions: [BPA] = 100 μM, [PMS] = 1 mM; [Catalyst] = 0.3 g L⁻¹).

be also observed, which was typically derived from Fe^{III} high-spin geometries with large zero-field splitting. Similarly, the addition of PMS also improved the signal strength, implying the accelerated catalysis process accompanied by the iron states conversion, which was accordance with the previous research result reported by Dashdorj et al. [48]. Above variations obtained by EPR spectra manifested a stable and efficient Fe^{III}/Fe^{II} redox reaction in MP-3/PMS system.

In addition to EPR measurement, the variation of metal sites was also evaluated using XPS spectra. As depicted in Fig. 5d, compared with fresh sample, the relative portion of Fe^{II} in used sample slightly decreased accompanied by the increased content of Fe^{III} species, manifesting the participation of Fe-NC sites into organics oxidation and consequent redox transformation. Nevertheless, the existence of metallic iron in the bulk phase could efficiently improve the catalyst electrical conductivity and facilitate electron-shuttling during catalysis process, confirmed by EIS and open-circuit voltage analysis (Fig. S12c), showing significant auxiliary contribution to catalytic kinetic process.

3.4.2. Mechanistic insight into direct singlet oxygen-mediated mechanism

Proverbially, quenching experiments in the complete solvent substitution experiment (MeOH → H₂O, Fig. 6a), L-histidine showed stronger inhibition effect than DMSO scavenger, indicating the more crucial participatory role of singlet oxygen than that high valent iron species (Fig. S16a). Besides, the typically improved EPR signal of TEMP-¹O₂ (1:1:1) under MeOH solvent system than pure PMS (Fig. S16b), further validated the dominant ¹O₂ species. It was demonstrated that ionization potential (IP) of organic pollutant can be regarded as an efficient descriptor to evaluate the redox capability of an oxidative system [49,50]. Herein, the redox capability of MP-3/PMS system was assessed by oxidation of various organic compounds with different IP values (BA, NB, BPA, HBA and PN), as shown in Table S1 and Fig. S17a-b. Obviously, the organic compounds with higher IP value

above 9.0 eV (BA and NB) were hardly decomposed, while the compounds with lower IP (BPA, HBA and PN < 9.0 eV) value exhibited higher reaction rate in MP-3/PMS system (Fig. 6b). This phenomenon was in accordance well with the results reported by Duan et al. [37], which was mainly attributed to that the surface confined metastable ¹O₂ nonradical with relatively low redox potential and selectivity cannot efficiently attack the organics with higher IP value. The similar results were also illustrated in nonradical ¹O₂ dominated PMS/PDS activation process with the addition of CuO-MgO/Fe₃O₄ [51] and β-MnO₂ [52] catalysts. Notably, the selective degradation of pollutants with different molecular structures in the reaction system of mixed pollutants once again verified unique advantage of ¹O₂ (Fig. S17c-e).

Considering the various evolutionary pathways of ¹O₂ production, such as self-decomposition of PMS, interaction between lattice oxygen and PMS, transformation of O₂^{·-}, interaction between PMS and ketonic/carbonyl group and photoexcited conversion of molecular oxygen [52], the derivation of ¹O₂ in MP-3/PMS system should be systematically explored and elucidated. Herein, due to the sluggish reaction rate and weak EPR signal of TEMP-¹O₂ adducts in pure PMS system, the contribution of PMS self-decomposition can be firstly ruled out. Besides, as an important intermediate species, O₂^{·-} can be transformed into ¹O₂ via direct oxidation reaction (O₂^{·-} + 2 H₂O → ¹O₂ + H₂O₂ + 2OH⁻). To identify this process, the EPR measurement was carried out with addition of DMPO quencher in the presence of MeOH. As shown in Fig. S16c, no characteristic sextet peaks of DMPO-O₂^{·-} complex can be observed, further excluding the possible transformation route of O₂^{·-} to ¹O₂. Given the absence of ketonic/carbonyl groups and light, interaction between PMS and ketonic/carbonyl groups and photoexcited conversion of molecular oxygen can be ignored. The aforementioned analysis and results demonstrated that the generated ¹O₂ maybe originated from direct decomposition of PMS on Fe-NC sites via the interaction of two oxygen atoms from PMS, which effectively refrain from competitive

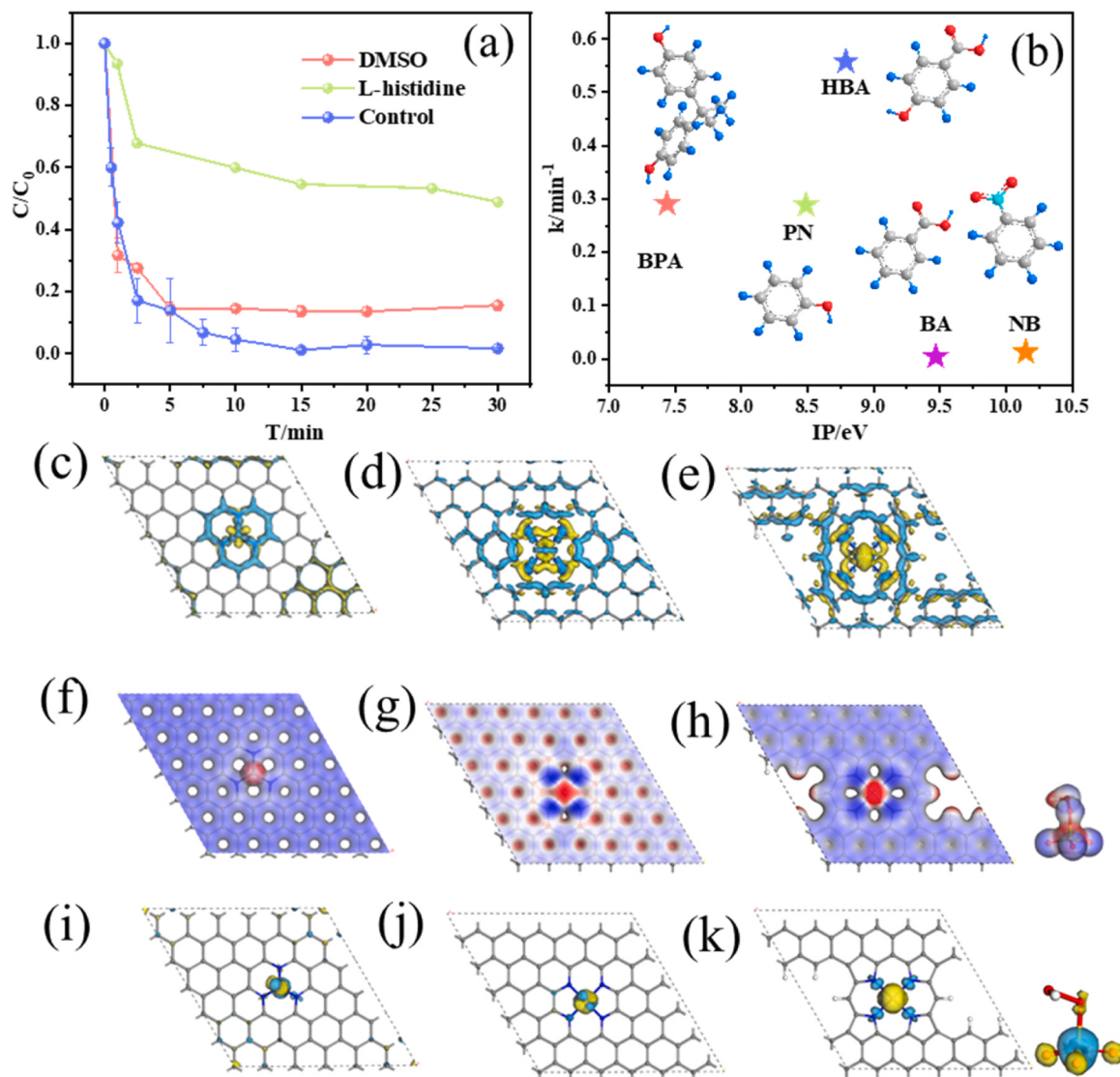


Fig. 6. Quenching experiment in MP-3/PMS system with methanol solvent (a) Relationship between organics degradation efficiency and corresponding ionization potentials (IP); (b) The charge density difference around the Fe atom embedded on Fe-graphitic N (c), Fe-pyridinic N (d) and Fe-pyrrolic N (e). The isosurface contour is $0.03 \text{ e}/\text{Bohr}^3$. The blue and yellow colors denote electron accumulation and depletion, respectively. The electrostatic potentials of PMS and Fe-graphitic N (f), Fe-pyridinic N (g) and Fe-pyrrolic N (h). The isosurface value is $0.15 \text{ e}/\text{Bohr}^3$. The spin density of PMS and Fe-graphitic N (i), Fe-pyridinic N (j) and Fe-pyrrolic N (k). The iso-surface value is $0.025 \text{ e}/\text{Bohr}^3$.

Haber-Weiss reaction ($\text{O}_2 + \text{H}_2\text{O}_2 \rightarrow \text{O}_2 + \text{H}_2\text{O} + \cdot\text{OH}$). In view of this hypothesis, DFT computations were carried out to systematically trace the origin of ${}^1\text{O}_2$ generation pathway and elucidate the possible direct ${}^1\text{O}_2$ -mediated mechanism via Fe-NC active moieties by Gibbs free energies (ΔG) profiles. The detailed theoretical methodology was described in Text S6. Firstly, three different Fe-NC models were optimized including Fe-graphitic, Fe-pyridinic and Fe-pyrrolic (Fig. S18). To elucidate the exact active sites, a detailed analysis of electronic structure was performed, which clearly showed that N atoms could accumulate electrons while electrons near Fe atoms were deficient. As a result, the Fe site was more likely to gain electrons from oxidant and achieve efficient PMS decomposition (Fig. 6c-e). Further, the electrostatic potentials of Fe-NC catalysts and PMS indicated that PMS has negative electrostatic potential on terminal O atoms, which can make them feasibly attract the site with positive electrostatic potential. On the surface of Fe-graphitic N, Fe-pyridinic N and Fe-pyrrolic N, the region around the Fe atoms had the most positive electrostatic potential value (Fig. 6f-h). Besides, there was strong magnetic interaction between Fe atom and PMS in water. As presented in Fig. 6i-k, both PMS and Fe

atoms had high spin polarization, providing a more active site than the C and N atoms for PMS adsorption and activation. According to the above analysis, Fe site turned out to be the most active site for PMS adsorption and activation. More in-depth investigations were needed to clarify which configuration was more likely to activate PMS to produce ${}^1\text{O}_2$ and detailed pathway.

In the experimental exploration, ${}^1\text{O}_2$ -induced oxidation pathway was identified as dominant reaction routine in Fe-NC/PMS system. During this process, PMS may undergo different intermediates to produce ${}^1\text{O}_2$ species on the possible adsorption configurations (Fe-graphitic N, Fe-pyridinic N and Fe-pyrrolic N) in Fe-NC catalyst. Therefore, the possible existed intermediate structures and corresponding energy profiles for ${}^1\text{O}_2$ formation were systematically calculated and elucidated in this work. It was known that the peroxy bond (O-O) in PMS is more easily evoked by electron transfer from Fe-graphitic N moiety to generate hydroxyl radicals ($\cdot\text{OH}$) and sulfate radical ($\text{SO}_4^{\cdot-}$) species instead of singlet oxygen [19]. Therefore, further corresponding activation mode were carried out using Fe-pyridinic N and Fe-pyrrolic N configurations. Based on this, the structure of PMS adsorption on Fe-

pyridinic N and Fe-pyrrolic N configurations were optimized and presented in Fig. 7a-b. The corresponding adsorption energies (E_{ads}) were calculated to be -2.45 and 2.22 eV, respectively, reflecting that PMS molecule is prone to interact with Fe-pyrrolic N configuration. Further, the charge density difference also indicated higher electron transfer (0.44 eV) between PMS and Fe-pyridinic N compared with Fe-pyrrolic N, reflecting the effective electron accumulation and chemisorption nature between PMS and Fe-pyridinic N moiety (Fig. 7a-b and Fig. S19a). The activation and conversion of PMS have three possible pathways for producing $^1\text{O}_2$ described in the Eqs. (1)–(5) [53]. In the pathway 1, the generation of $^1\text{O}_2$ occurred through the interaction of two oxygen atoms from two PMS molecules adsorbed on FeN_4 sites, while the remaining HSO_3^- combined with another HSO_5^- to form two HSO_4^- molecules (Eqs. (1) and (2)). In pathway 2 and 3, the HSO_5^- removed H to form SO_5^- and then reacted with another SO_5^- to generate $^1\text{O}_2$ and $\text{S}_2\text{O}_8^{2-}/\text{SO}_4^{2-}$ (Eqs. (3)–(5)). If the oxygen atoms were derived from same PMS molecule, the electrostatic repulsion between oxygen atoms with negative charge ($-0.53e \sim -0.67e$) is infeasible to $^1\text{O}_2$ production. Conversely, the S atoms in PMS with positive charge ($3.4e \sim 3.6e$) have potential to interact with O atoms, which showed enlarged

S-O bond length in the attached PMS than that of free PMS. Fig. 7c-d illustrated the potential energy surface of PMS activation on Fe-pyridinic/pyrrolic N sites to unravel the possible pathway of $^1\text{O}_2$ formation, and their reaction energies were given in Table S10. It can be clearly seen that Path 1 is the most readily and easier to happen with all three exothermic steps. Typically, compared with Fe-pyrrolic N moiety, Fe-pyridinic N exhibited the lowest energy barrier in each state towards $^1\text{O}_2$ formation, indicating the most thermodynamically favored reaction routine. Notably, when the second PMS molecule was adsorbed on Fe-pyridinic N site, the S-O bond length in the attached PMS (1.717 \AA) became longer than that of previous step (1.709 \AA), providing solid evidence for $^1\text{O}_2$ generation via pathway 1 (Fig. 7e-f).

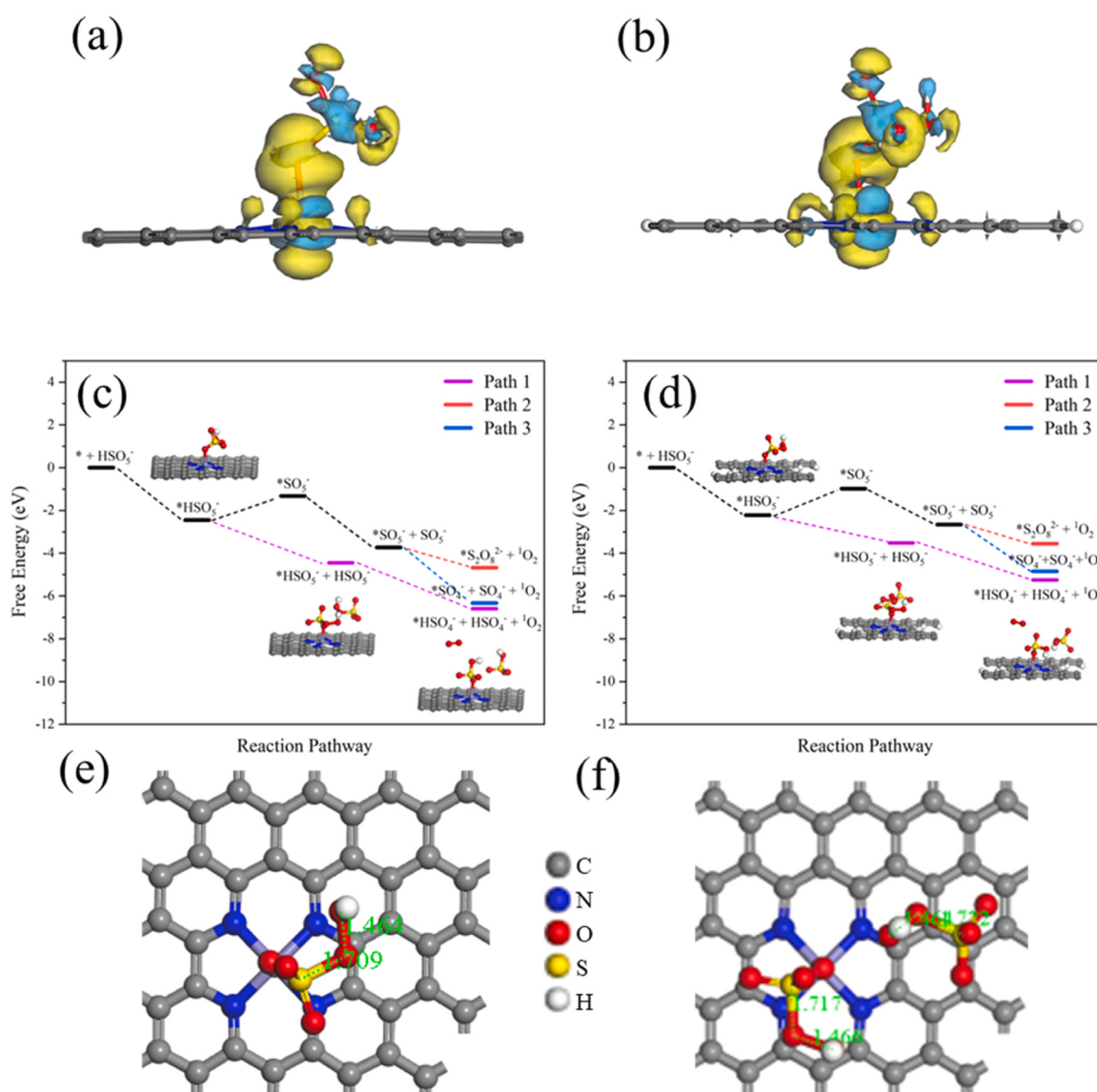
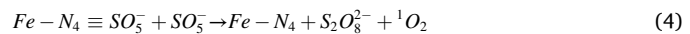
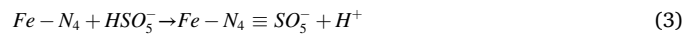
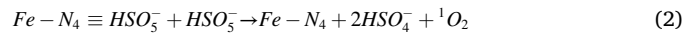


Fig. 7. The charge density difference around the PMS adsorbed on Fe-pyridinic N (a) and Fe-pyrrolic N (b). Potential energy surface of PMS activation on Fe-pyridinic N (e) and Fe-pyrrolic N (f) for generation of $^1\text{O}_2$. Optimized configurations and bond lengths of Fe-pyridinic N adsorbs one PMS molecule (e) and two PMS molecules (f).



Based on the above experimental analysis and DFT calculation, a novel 1O_2 dominated catalytic mechanism in reaction system was illustrated (Fig. 8). Firstly, PMS molecules bonded on the reactive FeN_4 sites by a terminal O atom of HSO_5^- , and the remaining HSO_3^- moieties interacted with another HSO_5^- . Subsequently, the S atom of HSO_5^- attached on the FeN_4 sites with positive charge could attract the O atom of free HSO_5^- moieties to generate two HSO_4^- . Ultimately, the two O atoms from adsorbed HSO_5^- can be further directly converted into 1O_2 . Benefiting from this effective process with lower potential energy, the nonradical 1O_2 specie played a pivotal role in PMS activation and pollutants oxidation.

3.5. Practical application potential

To reveal the decomposition ability of BPA by synthesized MP-3 catalyst, the degradation intermediates were investigated using FT-ICR-MS measurement and the possible degradation pathway was proposed accordingly. As depicted in Fig. S21 and Table S11, fourteen intermediates obtained from three chromatograms under different moments were identified. The substrate with m/z of 227 was assigned to BPA molecule. On the basis of decomposition intermediates, the conceivable degradation pathway of BPA over MP-3 catalyst was illustrated in Fig. S22. These processes were accordance well with that previously reported BPA decomposition intermediates [36,54–58].

In actual industrial effluents, various inorganic anions and natural organic matter (NOM) including humic acid (HA), halide ions and oxyanions could result in an obvious decline on contaminants removal efficiency through inactivating free radicals to generate low active anion radicals [59,60]. Herein, the BPA degradation in presence of five different anions (halide ions Cl^- and four common oxyanions SO_4^{2-} , HPO_4^{2-} , HCO_3^- , CO_3^{2-}) and HA in MP-3/PMS system was systematically evaluated. The concentration of these five anions was chosen as 10–1000 mM, which are far higher than any previously reported concentration (1 mM or 10 mM) and even close to the saturation concentration of anion salts. As shown in Fig. 9a, unlike the free radicals dominated system, the introduction of halide ions Cl^- boosted the catalytic process and improved removal efficiency, particularly under high concentration of Cl^- (1000 mM), which showed excellent potential for the treatment of highly salinity wastewater (Fig. S23a). Previous studies reported that the presence of Cl^- in Cl^- /PMS system can improved the decomposition efficiency of 2,4-DCP, cetirizine and dyes, owing to that

halide ions can react with SO_4^{2-} radical and PMS to generate halide radicals ($E(Cl_2\cdot/Cl^-) = 2.2 V_{NHE}$, $E(Cl\cdot/Cl^-) = 2.5 V_{NHE}$) and HOCl ($HSO_5^- + Cl^- \rightarrow SO_4^{2-} + HClO$) intermediate with longer lifetime and high oxidation potential (1.389 V)⁴. To reveal the specific role of Cl^- in MP-3/PMS system, the BPA degradation without catalyst addition was evaluated (Fig. S24a). Inscrutably, the BPA degradation was achieved in Cl^- /PMS system and the BPA can be decomposed instantaneously when the concentration of Cl^- reached to 100 mM and 1000 mM. Given the efficient degradation was attributed to Cl^- -generated from $\cdot OH$ and SO_4^{2-} and HOCl generated from PMS, the radical quenching experiments was performed to investigate the dominated role in reaction process. As shown in Fig. S24b, no significant inhibitory effect was observed in Cl^- /PMS/MeOH and MP-3/ Cl^- /PMS/MeOH systems, ruling out the role of Cl^- . These results revealed that the synergistic effect between Cl^- and MP-3 accelerated the degradation of BPA.

Besides, persulfate can be directly activated by HCO_3^- , CO_3^{2-} and HPO_4^{2-} ions to produce peroxyanions with lower redox capacity. However, in MP-3/PMS system, the catalytic activity was not inhibited after addition of high concentration of HPO_4^{2-} , HCO_3^- and CO_3^{2-} ions (Fig. 7c-e). Considering the characteristic of buffer reagents of these ions, the promoted catalytic kinetics may be ascribed to the adjustment of pH microenvironment. Meanwhile, it was noted that the k value in the presence of CO_3^{2-} was much higher than that of HCO_3^- under the same concentration of ions, which was likely due to the higher ionization constant of CO_3^{2-} and more significant improvement of system pH value. The variation of pH in MP-3/PMS system with different peroxyanions was measured and displayed in Fig. S25. Notably, the addition of three peroxyanions effectively regulated the microenvironment to alkaline condition. Compared with CO_3^{2-} and HPO_4^{2-} , equal concentration of HCO_3^- had less effect on system. With the increase of CO_3^{2-} and HPO_4^{2-} addition amount, the pH of reaction system gradually increased accompanied by the gradually decreased reaction activity due to the rapid PMS consumption by the excessive anions. On the contrary, compared with the consumption of PMS by HCO_3^- , the increase of pH boosted the reaction activity more effectively. This phenomenon was consistent with the analysis of pH parameter influence especially under alkaline condition pH = 9.18. Previous study had reported the SO_4^{2-} reduced the oxidation reduction potential of SO_4^{2-}/SO_4^{2-} , resulting in the decline of reaction efficiency [61,62]. However, due to the dominant role of non-radical pathways, the addition of SO_4^{2-} almost did not affect the catalytic reaction. Moreover, the complexation behavior of PMS on MP-3 catalyst was studied at different ionic strengths. As shown in Fig. S23f, the increasing ionic strengths had no effect on the degradation of BPA, indicating the

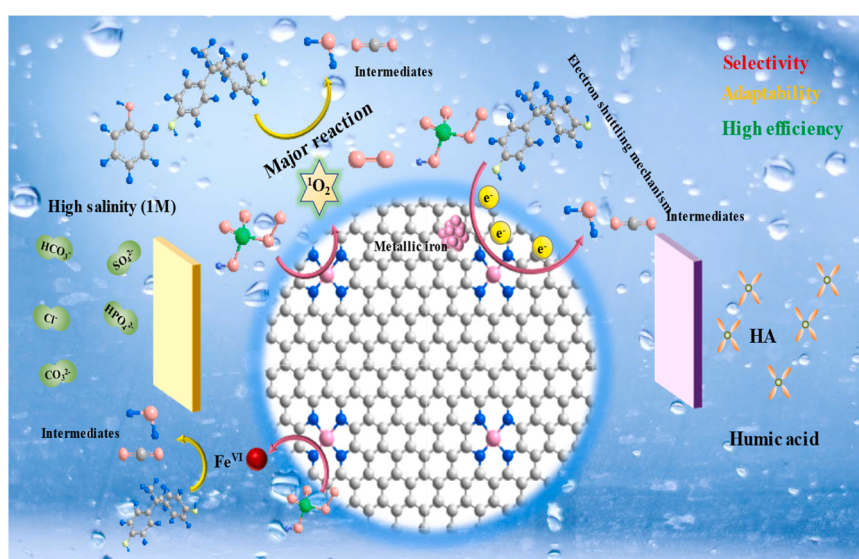


Fig. 8. Schematic of refractory organics degradation in MP-3/PMS system.

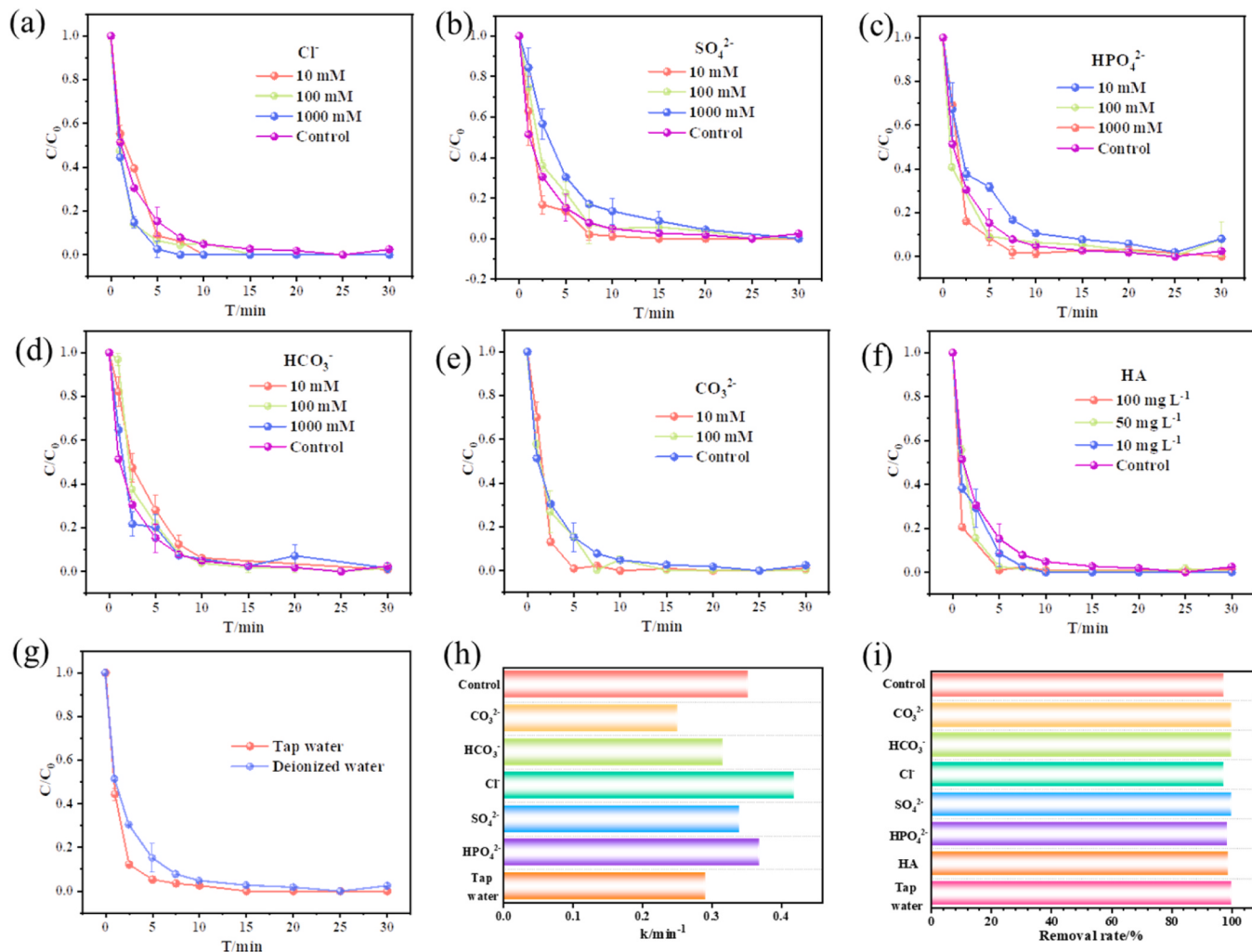


Fig. 9. Effect of different anions SO_4^{2-} (a); HPO_4^{2-} (b); HCO_3^- (c); Cl^- (d); CO_3^{2-} (e); different concentration HA (f); different water quality (g) on the BPA degradation by the MP-3/PMS system. Comparison of reaction kinetics in the presence of different substrates (h); Comparison of BPA removal rate in the presence of different substrates (i). (Conditions: [BPA] = 100 μM , [PMS] = 1 mM; [Catalyst] = 300 mg L^{-1}).

existence of inner-sphere complexation (covalent or ionic bonding) between MP-3 and PMS. Unlike outer-sphere complexation (electrostatic interaction), the strong inner-sphere complexation could exhibit better resistance for external impurities, which was consistent with the above results. Notably, the effect of several cations including, Na^+ , K^+ , Ca^{2+} and Mg^{2+} on the degradation performance was explored in reaction system. As shown in Fig. S25a, the existence of Ca^{2+} , Na^+ , Mg^{2+} and K^+ only showed negligible influence on the removal efficiency, further indicating the superior resistance of realistic wastewater matrixes and the practical application in the further environmental remediation.

Additionally, as a macromolecular organic matter, HA with carboxyl and phenolic hydroxyl group can also influence the acid-base property and deactivate free radicals with high kinetic constant rate. However, in MP-3/PMS system, the addition of HA accelerated the organic compounds oxidation process instead of inhibiting the removal efficiency (Figs. 7f and S26a). To trace the intrinsic essence of this phenomenon, the fluctuation of pH during catalysis was monitored. As depicted in Fig. S26b, the addition of HA only slightly decreased pH value within a limited scale (0.1~0.3), excluding the influence of microenvironment by HA. Previous studies demonstrated that HA could improve wastewater decontamination efficiency in $\text{H}_2\text{O}_2\text{-Fe}^{\text{III}}$ system via coordinating stage and thus accelerate the $\text{Fe}^{\text{III}}/\text{Fe}^{\text{II}}$ redox conversion [55]. Similarly, the HA/PMS system without iron-based catalyst exhibited sluggish BPA degradation efficiency (Fig. S26c), which is distinctly different from

control MP-3/PMS group. Owing to the similar structure between H_2O_2 and PMS oxidants, the reinforcement of reaction efficiency in MP-3/PMS system may be ascribed to the interaction between HA and iron sites on MP-3 catalyst surface, further accelerating the traditional rate-limiting step of Fenton-like process. These results evidently revealed the excellent resistance to high-salty wastewater containing inorganic anions and organic matter. Additionally, the superior anti-interference to inorganic/organic species was also achieved in real tap water substrate by MP-3 catalyst, substantiating the high adaptability in the future practical environment remediation (Figs. 9g and S27). In summary, as shown in Fig. 9h-i, Although the reaction kinetics had undergone certain changes, it still maintained high reaction efficiency. Notably, the removal rate of BPA was not disturbed by various substrates in reaction system and still can reached almost 100% in 10 min.

The stability and reusability of MP-3 catalyst were assessed by five consecutive cycling tests. As displayed in Fig. S28a, the degradation results indicated that approximately 94.8% catalytic efficiency can be still fulfilled by MP-3 catalyst after five cycles. The slight attenuation of removal rate was inevitable and may be mainly attributable to the adsorption of decomposition intermediates on the surface-active sites, irreversible iron leaching loss and partial conversion from graphitic N to pyrrolic N (obtained by XPS analysis). However, the total leached iron ions concentration was measured to be only 0.40 mg L^{-1} by ICP-OES, which seems to be rather limited and negligible during cyclic

experiment. The changes in the relative proportion of different iron species are insignificant, verifying the stability of FeNx catalyst during the reaction (Fig. S28c-d). To further evaluate the potential application of FeNx/PMS system, a continuous wastewater treatment was performed [63]. As shown in Fig. S29, the MP-3 catalyst was loaded onto the fibrous membrane. The MP-3 membrane was clamped to a rubber ring and supporting plate with abundant hole (diameter 2 mm) for pollutant degradation. RhB was selected as model pollutant to evaluate the reaction efficiency in MP-3 membrane/PMS system, which is intuitive to observe and recognize. It can be clearly seen that pristine MP-3 membrane only showed negligible removal efficiency towards RhB pollutant due to the adsorption effect (Fig. S29). Differently, the co-existence of MP-3 catalyst on membrane and PMS can efficiently elevate the pollutant degradation efficiency and only showed slight decline after 480 min consecutive reaction (the removal rate can maintain at ~72%), indicating certain stability and reusability for further practical application. The negligible variation of crystal (XRD) in MP-3 catalyst before and after reaction validated no aggregation of iron species on the catalyst surface during PMS activation process (Fig. S28b). These findings collectively manifested the excellent stability and reusability of as-synthesized Fe-NC catalyst during Fenton-like reaction towards environment purification.

4. Conclusion

In summary, Fe-based catalyst was fabricated by adjusting the ratio of PB and melamine. Benefiting from the inherited conductive property of iron nanocluster species and high activity of single iron atom, MP-3 catalyst delivered superior catalytic activity in PMS activation for refractory pollutant degradation even under high salinity, high concentration of humic acid and wide pH range, tackling the intractable challenges from classical PMS-based AOPs. Quenching experiment and EPR measurement indicated the dominant nonradical $^1\text{O}_2$ specie, while electron shuttling and high-valent iron-oxo species played auxiliary contribution. Unlike the previously indirect evolution pathway of $^1\text{O}_2$ through the conversion of precursor ($\cdot\text{O}_2$, SO_5^-), experimental and computational results collectively authenticated the vital role of FeN₄ moieties. Based on the comparison of three generation pathway of $^1\text{O}_2$ at different FeN₄ configuration, it was proposed the detailed direct $^1\text{O}_2$ mediated generation pathway occurred through the interaction of two O atoms from adsorbed PMS (HSO_5^-) molecule, accompanying two HSO_4^- molecules generation with the lowest energy barrier. This study provided atomic-scale understanding of catalytic mechanism in the PMS-assisted $^1\text{O}_2$ generation via FeN₄ sites, offering new insight for developing high efficiency, high selectivity and high adaptability Fenton-like catalysts in future environmental remediation.

CRediT authorship contribution statement

Liang Zhang: Data curation, Formal analysis, Methodology, Software, Writing – original draft. **Yun Sun:** Theoretical calculation, Writing – review & editing. **Rile Ge:** Visualization, Writing – review & editing. **Wenhui Zhou:** Writing – review & editing, Validation. **Zhimin Ao:** Supervision, Conceptualization, Methodology. **Junhu Wang:** Funding acquisition, Project administration, Supervision.

Declaration of Competing Interest

The authors declare that they have no known competing financial interests or personal relationships that could have appeared to influence the work reported in this paper.

Data availability

No data was used for the research described in the article.

Acknowledgments

This work was financially supported by the National Natural Science Foundation of China (U22A20394, 21961142006), the International Partnership Program of Chinese Academy of Sciences (121421KYSB20170020) and National Key R&D Program of China (No. 2022YFC3901800). The authors would like to thank Dr. Zoltán Klencsár for the analysis of the Mössbauer spectrum. The authors wish to thank Lirong Zheng and Wei Xu for the measurement and analysis of X-ray absorption spectroscopy.

Appendix A. Supplementary material

Supplementary data associated with this article can be found in the online version at doi:10.1016/j.apcatb.2023.123130.

References

- [1] B.-T. Zhang, Y. Zhang, Y. Teng, M. Fan, Sulfate radical and its application in decontamination technologies, Crit. Rev. Environ. Sci. Technol. 45 (16) (2014) 1756–1800.
- [2] S. Xiao, M. Cheng, H. Zhong, Z. Liu, Y. Liu, X. Yang, Q. Liang, Iron-mediated activation of persulfate and peroxymonosulfate in both homogeneous and heterogeneous ways: a review, Chem. Eng. J. 384 (2020) 123265–123289.
- [3] P. Shao, Y. Jing, X. Duan, H. Lin, L. Yang, W. Ren, F. Deng, B. Li, X. Luo, S. Wang, Revisiting the graphitized nanodiamond-mediated activation of peroxymonosulfate: singlet oxygenation versus electron transfer, Environ. Sci. Technol. 55 (23) (2021) 16078–16087.
- [4] J. Lee, U. von Gunten, J.H. Kim, Persulfate-based advanced oxidation: critical assessment of opportunities and roadblocks, Environ. Sci. Technol. 54 (6) (2020) 3064–3081.
- [5] Y. Zhang, M. Zhou, A critical review of the application of chelating agents to enable Fenton and Fenton-like reactions at high pH values, J. Hazard. Mater. 362 (2019) 436–450.
- [6] L. Wu, Z. Sun, Y. Zhen, S. Zhu, C. Yang, J. Lu, Y. Tian, D. Zhong, J. Ma, Oxygen vacancy-induced nonradical degradation of organics: critical trigger of oxygen (O_2) in the Fe-Co LDH/peroxymonosulfate system, Environ. Sci. Technol. 55 (22) (2021) 15400–15411.
- [7] X. Zhang, Z. Yao, J. Wang, W. Guo, X. Wu, Z. Jiang, High-capacity NCNT-encapsulated metal NP catalysts on carbonised loofah with dual-reaction centres over C–M bond bridges for Fenton-like degradation of antibiotics, Appl. Catal. B Environ. 307 (2022) 121205–121216.
- [8] X. Zhou, M.K. Ke, G.X. Huang, C. Chen, W. Chen, K. Liang, Y. Qu, J. Yang, Y. Wang, F. Li, H.Q. Yu, Y. Wu, Identification of Fenton-like active Cu sites by heteroatom modulation of electronic density, Proc. Natl. Acad. Sci. USA 119 (8) (2022) e2119492119–e2119492127.
- [9] W. Ye, S. Chen, Y. Lin, L. Yang, S. Chen, X. Zheng, Z. Qi, C. Wang, R. Long, M. Chen, J. Zhu, P. Gao, L. Song, J. Jiang, Y. Xiong, Precisely tuning the number of Fe atoms in clusters on N-doped carbon toward acidic oxygen reduction reaction, Chem 5 (11) (2019) 2865–2878.
- [10] Y. Jia, X. Xiong, D. Wang, X. Duan, K. Sun, Y. Li, L. Zheng, W. Lin, M. Dong, G. Zhang, W. Liu, X. Sun, Atomically dispersed Fe-N₄ modified with precisely located S for highly efficient oxygen reduction, Nano-Micro Lett. 12 (1) (2020) 1–13.
- [11] C.C. Hou, L. Zou, L. Sun, K. Zhang, Z. Liu, Y. Li, C. Li, R. Zou, J. Yu, Q. Xu, Single-atom iron catalysts on overhang-eave carbon cages for high-performance oxygen reduction reaction, Angew. Chem. Int. Ed. 59 (19) (2020) 7384–7389.
- [12] C. Chu, Q. Zhu, Z. Pan, S. Gupta, D. Huang, Y. Du, S. Weon, Y. Wu, C. Muhić, E. Stavitski, K. Domén, J.H. Kim, Spatially separating redox centers on 2D carbon nitride with cobalt single atom for photocatalytic H_2O_2 production, Proc. Natl. Acad. Sci. USA 117 (12) (2020) 6376–6382.
- [13] W. Qu, X. Liu, J. Chen, Y. Dong, X. Tang, Y. Chen, Single-atom catalysts reveal the dinuclear characteristic of active sites in NO selective reduction with NH_3 , Nat. Commun. 11 (1) (2020) 1532–1539.
- [14] Y. Gao, Y. Zhu, T. Li, Z. Chen, Q. Jiang, Z. Zhao, X. Liang, C. Hu, Unraveling the high-activity origin of single-atom iron catalysts for organic pollutant oxidation via peroxymonosulfate activation, Environ. Sci. Technol. 55 (12) (2021) 8318–8328.
- [15] J. He, Y. Wan, W. Zhou, ZIF-8 derived Fe-N coordination moieties anchored carbon nanocubes for efficient peroxymonosulfate activation via non-radical pathways: role of FeN(x) sites, J. Hazard. Mater. 405 (2021), 124199.
- [16] L. Wang, J. Jiang, S.-Y. Pang, Y. Zhou, J. Li, S. Sun, Y. Gao, C. Jiang, Oxidation of bisphenol A by nonradical activation of peroxymonosulfate in the presence of amorphous manganese dioxide, Chem. Eng. J. 352 (2018) 1004–1013.
- [17] J. Ji, Q. Yan, P. Yin, S. Mine, M. Matsuoka, M. Xing, Defects on CoS_{2-x} : tuning redox reactions for sustainable degradation of organic pollutants, Angew. Chem. Int. Ed. 60 (6) (2021) 2903–2908.
- [18] S. Wang, Y. Liu, J. Wang, Peroxymonosulfate activation by Fe-Co-O-codoped graphite carbon nitride for degradation of sulfamethoxazole, Environ. Sci. Technol. 54 (16) (2020) 10361–10369.

- [19] J. Hu, X. Zeng, G.B. Qian, Y. Liu, X. Hu, B. He, L. Zhang, X. Zhang, Modulating mesoporous Co_3O_4 hollow nanospheres with oxygen vacancies for highly efficient peroxymonosulfate activation, *Chem. Eng. J.* 400 (2020) 125869.
- [20] C. Dong, Y. Bao, T. Sheng, Q. Yi, Q. Zhu, B. Shen, M. Xing, I.M.C. Lo, J. Zhang, Singlet oxygen triggered by robust bimetallic MoFe/TiO_2 nanospheres of highly efficacy in solar-light-driven peroxymonosulfate activation for organic pollutants removal, *Appl. Catal. B Environ.* 286 (2021) 119930–119942.
- [21] L. Yang, H. Yang, S. Yin, X. Wang, M. Xu, G. Lu, Z. Liu, H. Sun, Fe single-atom catalyst for efficient and rapid Fenton-like degradation of organics and disinfection against Bacteria, *Small* 18 (2022) e2104941–e2104955.
- [22] M. Li, Z. Li, X. Yu, Y. Wu, C. Mo, M. Luo, L. Li, S. Zhou, Q. Liu, N. Wang, K. Lun Yeung, S. Chen, FeN_4 -doped carbon nanotubes derived from metal organic frameworks for effective degradation of organic dyes by peroxymonosulfate: Impacts of FeN_4 spin states, *Chem. Eng. J.* 431 (4) (2021) 133339–133351.
- [23] J. Liu, X. Li, B. Liu, C. Zhao, Z. Kuang, R. Hu, B. Liu, Z. Ao, J. Wang, Shape-controlled synthesis of metal-organic frameworks with adjustable Fenton-Like catalytic activity, *ACS Appl. Mater. Interfaces* 10 (44) (2018) 38051–38056.
- [24] X. Yu, L. Wang, X. Wang, H. Liu, Z. Wang, Y. Huang, G. Shan, W. Wang, L. Zhu, Enhanced nonradical catalytic oxidation by encapsulating cobalt into nitrogen doped graphene: highlight on interfacial interactions, *J. Mater. Chem. A* 9 (11) (2021) 7198–7207.
- [25] X. Li, K. Zhu, J. Pang, M. Tian, J. Liu, A.I. Rykov, M. Zheng, X. Wang, X. Zhu, Y. Huang, B. Liu, J. Wang, W. Yang, T. Zhang, Unique role of Mössbauer spectroscopy in assessing structural features of heterogeneous catalysts, *Appl. Catal. B Environ.* 224 (2018) 518–532.
- [26] U.I. Kramm, Z.I. Abs-Wurmback, I. Herrmann-Geppert, J. Radnik, S. Fiechter, P. Bogdanoff, Influence of the electron-density of FeN_4 -centers towards the catalytic activity of pyrolyzed FeTMPPCl-based ORR-electrocatalysts, *J. Electrochem. Soc.* 158 (2011) B69–B78.
- [27] L. Ni, C. Gallenkamp, S. Paul, M. Kübler, P. Theis, S. Chabarra, K. Hofmann, E. Bill, A. Schnegg, B. Albert, V. Krewald, U.I. Kramm, Active site identification in FeNC catalysts and their assignment to the oxygen reduction reaction pathway by *in situ* ^{57}Fe Mössbauer spectroscopy, *Adv. Energy Sustain. Res.* (2021) 2.
- [28] U.I. Kramm, L. Ni, S. Wagner, (^{57}Fe) Mossbauer spectroscopy characterization of electrocatalysts, *Adv. Mater.* 31 (2019), e1805623.
- [29] S. Wagner, H. Auerbach, C.E. Tait, I. Martinaiou, S.C.N. Kumar, C. Kubel, I. Sergeev, H.C. Wille, J. Behrends, J.A. Wolny, V. Schunemann, U.I. Kramm, Elucidating the structural composition of an Fe-N-C catalyst by nuclear- and electron-resonance techniques, *Angew. Chem. Int. Ed.* 58 (2019) 10486–10492.
- [30] U.I. Koslowski, I. Abs-Wurmback, S. Fiechter, P. Bogdanoff, Nature of the catalytic centers of porphyrin-based electrocatalysts for the ORR: a correlation of kinetic current density with the site density of Fe-N4 centers, *J. Phys. Chem. C* 112 (2008) 15356–15366.
- [31] B.A. Shaevitz, G. Lang, C.A. Reed, Susceptibility and Mossbauer analysis of a high-spin ferrous synthetic heme with unusually large quadrupole splitting, *Inorg. Chem.* 27 (1988) 4607–4613.
- [32] T.A. Wezendonk, V.P. Santos, M.A. Nasalevich, Q.S.E. Warringa, A.I. Dugulan, A. Chojecki, A.C.J. Koeken, M. Ruitenbeek, G. Meima, H.-U. Islam, G. Sankar, M. Makkee, F. Kapteijn, J. Gascon, Elucidating the nature of Fe species during pyrolysis of the Fe-BTC MOF into highly active and stable Fischer-Tropsch catalysts, *ACS Catal.* 6 (2016) 3236–3247.
- [33] W.T. Herrera, I. Dinola, E. Baggio-Saitovitch, M. Kraken, F.J. Litterst, Magnetic dynamics of dilute iron nano-clusters in silver films from Mössbauer spectroscopy and muon spin rotation, *Hyperfine Interact.* 203 (1–3) (2011) 149–153.
- [34] W.T. Herrera, Y.T. Xing, S.M. Ramos, P. Munayco, M.B. Fontes, E.M. Baggio-Saitovitch, F.J. Litterst, Kondo effect and spin-glass behavior of dilute iron clusters in silver films, *Phys. Rev. B* 84 (1) (2011), 014430, 1–7.
- [35] I.P. Suzdalev, Y.V. Maksimov, Critical sizes and characteristics of nanoclusters and nanostructures, *Hyperfine Interact.* 165 (1–4) (2006) 25–35.
- [36] L. Zhang, B. Zhang, L. Wang, R. Ge, W. Zhou, S. Kubuki, R. Wu, J. Wang, Self-assembly of MoS_2 nanosheet adhered on Fe-MOF heterocrystals for peroxymonosulfate activation via interfacial interaction, *J. Colloid Interface Sci.* 608 (Pt 3) (2022) 3098–3110.
- [37] M. Zhang, C. Xiao, X. Yan, S. Chen, R. Wang, C. Luo, J. Qi, X. Sun, L. Wang, J. Li, Efficient removal of organic pollutants by metal-organic framework derived Co/C yolk-shell nanoreactors: size-exclusion and confinement effect, *Environ. Sci. Technol.* 54 (2020) 10289–10300.
- [38] X. Peng, J. Wu, Z. Zhao, X. Wang, H. Dai, L. Xu, G. Xu, Y. Jian, F. Hu, Activation of peroxymonosulfate by single-atom Fe-g-C₃N₄ catalysts for high efficiency degradation of tetracycline via nonradical pathways: role of high-valent iron-oxo species and Fe-Nx sites, *Chem. Eng. J.* 427 (2022) 130803–130833.
- [39] H. Dong, Q. Xu, L. Lian, Y. Li, S. Wang, C. Li, X. Guan, Degradation of organic contaminants in the Fe(II)/peroxymonosulfate process under acidic conditions: The overlooked rapid oxidation stage, *Environ. Sci. Technol.* 55 (22) (2021) 15390–15399.
- [40] L. He, C. Yang, J. Ding, M.-Y. Lu, C.-X. Chen, G.-Y. Wang, J.-Q. Jiang, L. Ding, G.-S. Liu, N.-Q. Ren, S.-S. Yang, Fe, N-doped carbonaceous catalyst activating periodate for micropollutant removal: significant role of electron transfer, *Appl. Catal. B Environ.* 303 (2022) 120880–120894.
- [41] H. Lee, H.I. Kim, S. Weon, W. Choi, Y.S. Hwang, J. Seo, C. Lee, J.H. Kim, Activation of persulfates by graphitized nanodiamonds for removal of organic compounds, *Environ. Sci. Technol.* 50 (18) (2016) 10134–10142.
- [42] Y.-H. Li, C.-C. Wang, F. Wang, W. Liu, L. Chen, C. Zhao, H. Fu, P. Wang, X. Duan, Nearly zero peroxydisulfate consumption for persistent aqueous organic pollutants degradation via nonradical processes supported by *in-situ* sulfate radical regeneration in defective MIL-88B(Fe), *Appl. Catal. B Environ.* 331 (2023), 122699.
- [43] C. Zhao, L. Meng, H. Chu, J.-F. Wang, T. Wang, Y. Ma, C.-C. Wang, Ultrafast degradation of emerging organic pollutants via activation of peroxymonosulfate over Fe3C/Fe/N-C-x: singlet oxygen evolution and electron-transfer mechanisms, *Appl. Catal. B Environ.* 321 (2023), 122034.
- [44] K. Qian, H. Chen, W. Li, Z. Ao, Y.N. Wu, X. Guan, Single-atom Fe catalyst outperforms its homogeneous counterpart for activating peroxymonosulfate to achieve effective degradation of organic contaminants, *Environ. Sci. Technol.* 55 (2021) 7034–7043.
- [45] S. Wang, L. Xu, J. Wang, Iron-based dual active site-mediated peroxymonosulfate activation for the degradation of emerging organic pollutants, *Environ. Sci. Technol.* 55 (22) (2021) 15412–15422.
- [46] V.A. Saveleva, K. Ebner, L. Ni, G. Smolentsev, D. Klose, A. Zitolo, E. Marelli, J. Li, M. Medarde, O.V. Safonova, M. Nachtegaal, F. Jaouen, U.I. Kramm, T.J. Schmidt, J. Herranz, Potential-induced spin changes in Fe/N/C electrocatalysts assessed by *in situ* X-ray emission spectroscopy, *Angew. Chem. Int. Ed.* 60 (21) (2021) 11707–11712.
- [47] C. Citek, P.H. Oyala, J.C. Peters, Mononuclear Fe(I) and Fe(II) acetylene adducts and their reductive protonation to terminal Fe(IV) and Fe(V) carbynes, *J. Am. Chem. Soc.* 141 (38) (2019) 15211–15221.
- [48] J. Dashdorj, M.E. Zvanut, L.J. Stanley, Iron-related defect levels in SrTiO₃ measured by photoelectron paramagnetic resonance spectroscopy, *J. Appl. Phys.* 107 (8) (2010) 3513–3517.
- [49] S. Zhu, X. Li, J. Kang, X. Duan, S. Wang, Persulfate activation on crystallographic manganese oxides: mechanism of singlet oxygen evolution for nonradical selective degradation of aqueous contaminants, *Environ. Sci. Technol.* 53 (1) (2018) 307–315.
- [50] T. Zhang, H. Zhu, J.P. Crouse, Production of sulfate radical from peroxymonosulfate induced by a magnetically separable CuFe_2O_4 spinel in water: efficiency, stability, and mechanism, *Environ. Sci. Technol.* 47 (6) (2013) 2784–2791.
- [51] A. Jawad, K. Zhan, H. Wang, A. Shahzad, Z. Zeng, J. Wang, X. Zhou, H. Ullah, Z. Chen, Z. Chen, Tuning of persulfate activation from a free radical to a nonradical pathway through the incorporation of non-redox magnesium oxide, *Environ. Sci. Technol.* 54 (4) (2020) 2476–2488.
- [52] X. Zhou, Q. Zhao, J. Wang, Z. Chen, Nonradical oxidation processes in PMS-based heterogeneous catalytic system: generation, identification, oxidation characteristics, challenges response and application prospects, *Chem. Eng. J.* 410 (2021) 128312–128327.
- [53] J. Hu, Y. Li, Y. Zou, L. Lin, B. Li, X. Li, Transition metal single-atom embedded on N-doped carbon as a catalyst for peroxymonosulfate activation: A DFT study, *Chem. Eng. J.* 437 (2022) 135428–135439.
- [54] X. Li, Z. Wang, B. Zhang, A.I. Rykov, M.A. Ahmed, J. Wang, $\text{Fe}_x\text{Co}_{3-x}\text{O}_4$ nanocages derived from nanoscale metal-organic frameworks for removal of bisphenol A by activation of peroxymonosulfate, *Appl. Catal. B Environ.* 181 (2016) 788–799.
- [55] J. Xu, J. Song, Y. Min, Q. Xu, P. Shi, Mg-induced g-C₃N₄ synthesis of nitrogen-doped graphitic carbon for effective activation of peroxymonosulfate to degrade organic contaminants, *Chin. Chem. Lett.* 33 (6) (2022) 3113–3118.
- [56] T. Wang, J. Zhou, W. Wang, Y. Zhu, J. Niu, Ag-single atoms modified $\text{S}_{1.66}\text{Ni}_{1.91}/\text{TiO}_{2-x}$ for photocatalytic activation of peroxymonosulfate for bisphenol A degradation, *Chin. Chem. Lett.* 33 (4) (2022) 2121–2124.
- [57] Q. Chen, C. Yuan, C. Zhai, Label-free photoelectrochemical sensor based on 2D/2D $\text{ZnIn}_2\text{S}_4/\text{g-C}_3\text{N}_4$ heterojunction for the efficient and sensitive detection of bisphenol A, *Chin. Chem. Lett.* 33 (2) (2022) 983–986.
- [58] R. Zhang, M. Chen, Z. Xiong, Y. Guo, B. Lai, Highly efficient degradation of emerging contaminants by magnetic CuO@Fe_xO_y derived from natural mackinawite (FeS) in the presence of peroxymonosulfate, *Chin. Chem. Lett.* 33 (2) (2022) 948–952.
- [59] C. Chen, T. Ma, Y. Shang, B. Gao, B. Jin, H. Dan, Q. Li, Q. Yue, Y. Li, Y. Wang, X. Xu, In-situ pyrolysis of Enteromorpha as carbocatalyst for catalytic removal of organic contaminants: considering the intrinsic N/Fe in Enteromorpha and non-radical reaction, *Appl. Catal. B Environ.* 250 (2019) 382–395.
- [60] S. Yang, P. Wu, J. Liu, M. Chen, Z. Ahmed, N. Zhu, Efficient removal of bisphenol A by superoxide radical and singlet oxygen generated from peroxymonosulfate activated with Fe^0 -montmorillonite, *Chem. Eng. J.* 350 (2018) 484–495.
- [61] S. Naim, A. Ghauch, Ranitidine abatement in chemically activated persulfate systems: assessment of industrial iron waste for sustainable applications, *Chem. Eng. J.* 288 (2016) 276–288.
- [62] B. Yang, X. Cheng, Y. Zhang, W. Li, J. Wang, Z. Tian, E. Du, H. Guo, Staged assessment for the involving mechanism of humic acid on enhancing water decontamination using $\text{H}_2\text{O}_2\text{-Fe}(\text{III})$ process, *J. Hazard. Mater.* 407 (2021) 124853–124863.
- [63] X. Zhang, J. Liu, H. Zhang, Z. Wan, J. Li, Uncovering the pathway of peroxymonosulfate activation over $\text{Co}_{0.5}\text{Zn}_{0.5}\text{O}$ nanosheets for singlet oxygen generation: performance and membrane application, *Appl. Catal. B Environ.* 327 (61) (2023).